ABSTRACT

A hybrid pulse-tube/reverse-Brayton cryocooler is being developed that integrates a regenerative, pulse-tube upper temperature stage with a recuperative, reverse-Brayton lower temperature stage using a flow rectification system consisting of check-valves and buffer volumes. This system shows the potential for high performance with low mass and high reliability. Electrical, mechanical, and thermal integration with a load will be made easier by the continuous flow nature of the system. The turbine in the reverse-Brayton stage will be supported on hydrostatic gas bearings. The performance of the hybrid cryocooler system is strongly dependent upon the performance of these bearings; in particular their stiffness and mass flow consumption.

A theoretical bearing model was developed to predict journal bearing performance as a function of geometry and operating conditions. Following the development of the model, two single-admission hydrostatic gas journal bearings were fabricated, assembled, and integrated into a test bed. The test bed consisted of a fixture for the bearings, a shaft, a thrust bearing for axial support and a nozzle to spin the fully supported shaft in order to allow for rotordynamic testing. Instrumentation included pressure sensors and a fiber-optic sensor capable of measuring both shaft displacement and rotational frequency. The bearings were tested to validate the model and characterize their stiffness and mass flow consumption.

The model was used to optimize the bearing design for a hybrid cryocooler. It was found that an optimized bearing design did not maximize stiffness since this would require a high mass flow consumption which, in turn, would result in decreased cycle performance. Rather, in the optimized design, some stiffness was sacrificed in order to greatly reduce the mass flow consumption. Likewise, it was found that single admission bearings were optimal for the hybrid cycle, since mass flow consumption is minimized for a given stiffness. The bearing-to-shaft clearance was identified as a critical parameter for the optimized bearing design.

ACKNOWLEDGEMENTS

As with any endeavor, there are a great many people without whose help this work would never have come to be. They of course deserve many more thanks than can be conveyed in such short paragraphs as these.

First I would like to acknowledge my advisors Greg Nellis and John Pfotenhauer. I would like to thank Greg for bringing me into the solar lab, always making time for my questions, and making my experience most enjoyable. I would like to thank John for his patience and understanding, being available when needed, and his careful attention to the details of this research. Also, the other professors of the solar lab, specifically, Sandy Klein and his magnificent software, have been invaluable to this project and have helped expand my abilities as an engineer.

I would like to thank Jim Maddocks and Atlas Scientific for their support of this research. Likewise everyone in the liquid helium facility and the college of engineering machine shops, namely Orrie Lokken, Ed Dreier, and Bill Hagquist, have contributed many ideas to this project and have helped it become a success.

The 13th floor of ERB has been an interesting place to work and I will probably never have an office with such a nice view again and such nice people to work with. Extra special thanks are required for Seth Potratz and Mike Rothaupt who assisted me with my experiments. The graduate students of 1337 ERB (Brandon F. Lachner Memorial Jr. Memorial Graduate Student Office) along with all the students of the solar lab have made my stay most memorable and I wish them good luck in the future.

Finally I would like to thank my family for their years of support, love and encouragement. I would like to dedicate this work to them, specifically to my wife Kristin. For without her though my undergraduate and graduate years, this work would not have been a success.

This research has been financed by a Missile Defense Agency STTR Grant, Contract No F29601-02-C-0273 with technical support from the Cryogenics Group at Kirtland Air Force Base.

TABLE OF CONTENTS

ABSTRACT i
ACKNOWLEDGEMENTS iii
TABLE OF CONTENTS v
LIST OF FIGURES vii
LIST OF TABLES x
CHAPTER 1: INTRODUCTION
1.1 Regenerative Cryocoolers 1
1.2 Recuperative Cryocoolers 3
1.3 Hybrid Cryocooler Configurations 4
1.4 Motivation of Bearing Research 6
1.5 Project Objectives 7
CHAPTER 2: HYDROSTATIC BEARINGS
2.1 Description of Hydrostatic Bearings 8
2.2 Hydrostatic Bearing Model 10
2.3 Model Results with Air 18
2.3.1 Station Location Study 19
2.3.2 Number of Supply Holes Study 22
2.3.3 Supply Hole Radius Study 25
2.4 Model Results with Helium 26
2.4.1 Station Location Study 26
2.4.2 Number of Supply Holes Study 29
2.4.3 Supply Hole Radius Study 31
2.5 Comparison of Required Clearances 32
2.6 Prototype Bearing Design Summary 34
CHAPTER 3: FABRICATION OF A ROTORDYNAMIC SYSTEM
3.1 Test Fixture 35
3.1.1 Hydrostatic Journal Bearings 35
3.1.2 Housing 37
3.1.3 Thrust Bearing 39
3.1.4 Pneumatic Drive 41
3.2 Instrumentation 42
3.2.1 Mass Flow Sensor 44
3.2.2 Fiber-Optic Displacement Sensor 44
CHAPTER 4: EXPERIMENTAL RESULTS AND MODEL VALIDATION
4.1 Ambient Exhaust Pressure 47
4.2 Elevated Exhaust Pressure 48
4.3 Scaling Parameters 49

4.4 Shaft Rotational Speed Measurement 50

CHAPTER 5: BEARING OPTIMIZATION AND RESEARCH SUMMARY
5.1 Bearing Optimization for Hybrid Cryocooler 51
5.2 Bearing Research Summary 54
5.3 Recommendations for Further Bearing Research 55
5.4 Generation II Gas Bearing Test Facility 56

CHAPTER 6: HYBRID CRYOCOOLER PROTOTYPING
6.1 The Brassboard Concept 59
6.1.1 Brassboard Design Iteration 1 61
6.1.2 Brassboard Design Iteration 2 62
6.2 Vacuum Chamber (VaC) 63
6.2.1 Design 63
6.2.2 Fabrication 66
6.3 Vacuum Chamber Support Structure (VaCSS) 67
6.3.1 Design 67
6.3.2 Fabrication 69
6.4 Future Work 71

APPENDIX A: EES CODE FOR HYDROSTATIC BEARING MODEL 74

BIBLIOGRAPHY 76

LIST OF FIGURES

Figure 1.1: Orifice pulse-tube regenerative cryocooler 2
Figure 1.2: Reverse-Brayton recuperative cycle 3
Figure 1.3: Bootstrap configuration for hybrid OPT/RB cryocooler 5
Figure 1.4: Detailed schematic of hybrid pulse-tube/reverse-Brayton system 7
Figure 2.1: Pressurized gas bearings (double admission) 8
Figure 2.2: Resistive circuit analogy for hydrostatic bearings 9
Figure 2.3: Hydrostatic bearing schematic 10
Figure 2.4: Hydrostatic bearing model inputs for EES 12
Figure 2.5: Hydrostatic bearing model flowchart 13
Figure 2.6: Equivalent slot concept for a hydrostatic bearing 13
Figure 2.7: Slot height dependence on shaft/bearing centers 14
Figure 2.8: Stiffness scaling parameter vs. bearing pressure factor 18
Figure 2.9: $\dot{m}$ vs. r_h using air for various station 20
Figure 2.10: k vs. r_h using air for varying station 21
Figure 2.11: $k/\dot{m}$ vs. r_h using air for varying Station 22
Figure 2.12: $\dot{m}$ vs. r_h using air for varying number of supply holes 23
Figure 2.13: k vs. r_h using air for varying number of supply holes 24
Figure 2.14: $k/\dot{m}$ vs. r_h using air for varying number of supply holes 25
Figure 2.15: Effect of non-optimized r_h using Air (N=8) 26
Figure 2.16: $\dot{m}$ vs. r_h using cryogenic helium for varying station 27
Figure 2.17: k vs. r_h using cryogenic helium for varying station 28
Figure 2.18: $k/\dot{m}$ vs. r_h using cryogenic helium for varying station 28
Figure 2.19: $\dot{m}$ vs. r_h using cryogenic helium for varying number of feed holes 30
Figure 2.20: k vs. r_h using cryogenic helium for varying number of supply holes 30
Figure 2.21: $k/\dot{m}$ vs. r_h using cryogenic helium for varying number of supply holes 31
Figure 2.22: Effect of non-optimized r_h using cryogenic helium (N=8) 32
Figure 2.23: Mass flow rate vs. radial clearance comparison 33
Figure 2.24: Stiffness vs. radial clearance comparison 33

Figure 2.25: Prototype bearing design sketch 34
Figure 3.1: Integrated test fixture 35
Figure 3.2: Solid model of prototype bearing 36
Figure 3.3: Design drawing of bearing.....37
Figure 3.4: Housing body design drawing 38
Figure 3.5: Housing end cap design drawing.....39
Figure 3.6: Housing with basic components for horizontal operation 39
Figure 3.7: Thrust bearing design drawing 40
Figure 3.8: Fabricated thrust bearing 40
Figure 3.9: Nozzle-spacer drawing 41
Figure 3.10: Fabricated nozzle-spacer 42
Figure 3.11: Schematic of experimental setup 43
Figure 3.12: Experimental setup 43
Figure 3.13: Typical *Cole Parmer* mass flow sensor.....44
Figure 3.14: Typical *Philtec* fiberoptic sensor 45
Figure 3.15: RC12 *Philtec* fiberoptic sensor response curve 45
Figure 3.16: Typical impulse response from displacement sensor 46
Figure 3.17: Fiberoptic sensor fixture 46
Figure 4.1: Measured and predicted mass flow rate with ambient exhaust pressure 47
Figure 4.2: Measured and predicted stiffness with ambient exhaust pressure 48
Figure 4.3: Mass flow rate with elevated exhaust pressure (70 psig supply).....48
Figure 4.4: Stiffness with elevated exhaust pressure (60 psig supply) 49
Figure 4.5: Measured and predicted scaling parameters 49
Figure 4.6: Diameter etching on gage pin 50
Figure 4.7: Typical rotational speed measurement 50
Figure 5.1: 2nd law efficiency (%) as a function of scaling parameters C_m & C_k.....52
Figure 5.2: Optimization of hydrostatic bearings for the hybrid cryocooler 53
Figure 5.3: 2nd Law Efficiency (%) vs. radial clearance in the hydrostatic bearings 54
Figure 5.4: Generation II gas bearing test facility.....56
Figure 5.5: Mounting and instrumentation of test bearing.....57
Figure 5.6: Partial 3-D model of generation II gas bearing test facility.....58

Figure 6.1: Hybrid cryocooler research organization.....59
Figure 6.2: Conceptual drawing of brassboard concept.....60
Figure 6.3: Testing rig at Kirtland Air Force Base 62
Figure 6.4: Pulse tube/aftercooler interface with VaC.....65
Figure 6.5: Vacuum system schematic for VaC.....65
Figure 6.6: VaC specifications model showing important geometric specifications.....66
Figure 6.7: Vacuum chamber support structure bolt loading schematic.....68
Figure 6.8: Vacuum chamber outside support structure beam loading schematic.....69
Figure 6.9: Vacuum chamber support structure assembly 70
Figure 6.10: VaC and VaCSS assembly for brassboard cooler.....71

LIST OF TABLES

Table 6.1: Feedthru requirements for vacuum chamber 64
Table 6.2: Vacuum chamber support structure static load requirements.....67
Table 6.3: Bill of materials for vacuum chamber support structure 71
Table 6.4: Key project milestones.....72

CHAPTER 1

Introduction

This chapter describes types several types of cryocoolers and details the motivation and objectives of the research.

1.1 Regenerative Cryocoolers

Cryocoolers are refrigeration devices capable of achieving very low (below 120 K) temperatures. Today, both regenerative and recuperative cryocoolers are utilized. Figure 1 illustrates schematically a common configuration for a regenerative cryocooler, the orifice pulse-tube. Other regenerative cryocoolers include Stirling and Gifford-McMahon machines. These devices share the common characteristic of having a regenerative heat exchanger, a matrix of solid material that transfers heat to and from the oscillating working fluid during each cycle. The bulk of the working fluid in a regenerative cycle is pressurized in the compression space. This results in heat rejection in the compressor's aftercooler. Further cooling of the fluid occurs as it passes through the regenerator and exchanges heat with its matrix. The working fluid is then expanded in the cold space causing it to accept heat from the cold reservoir heat exchanger. The fluid is warmed by heat transfer from the matrix as it passes through the regenerator.

The efficiency of regenerative cryocoolers depends strongly on the performance of the regenerator. In order to attain high efficiency, it is necessary that the solid material have a high specific heat capacity relative to the working fluid to avoid large matrix temperature variations over a cycle. Most solids have diminished heat capacity at low temperature. Also, the density and therefore the mass of the fluid that is entrained in the regenerator matrix void volume becomes large as the temperature is reduced. These two effects make it difficult to fabricate regenerative cryocoolers that operate efficiently below about 20 K.

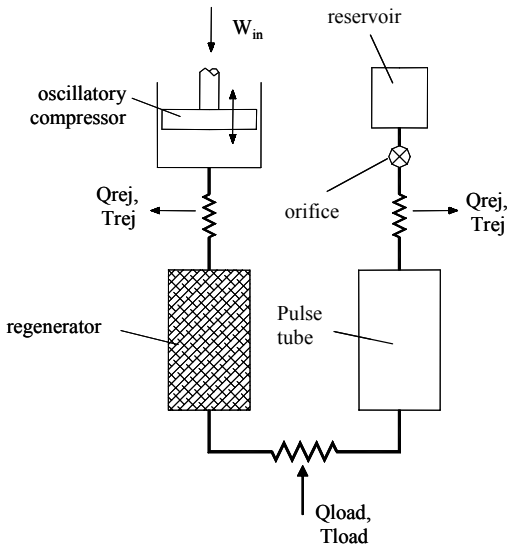

Figure 1.1: Orifice pulse-tube regenerative cryocooler

The orifice pulse-tube is a specific type of pulse-tube which is a specific type of regenerative cryocooler. Pulse-tube cryocoolers have attracted much interest not only because of their mechanical simplicity, but also for their reliability. Because they have no moving components in the low temperature regions, no source of vibration at the cold end (as opposed to Stirling coolers), and no critical valves subject to contamination or clogging (as opposed to the Joule-Thompson coolers) they appear to be very promising for space applications. Pulse-tubes have the additional advantage of operating at relatively low pressures over a wide range of frequencies. For all these reasons, application of pulse-tube technology in cryogenics is expected to expand in the near future.

The pulse-tube itself is a thin-walled stainless steel tube with copper heat exchangers at either end. The pulse-tube is joined to a regenerator, which is a stainless steel tube packed with a metal matrix typically comprised of screens. The assembly is contained in a vacuum vessel which limits thermal loses. The hot heat exchanger is enclosed in a water-cooled jacket. The operation of a pulse-tube involves compressing the gas and cooling it in an aftercooler. The gas flows through a regenerator and then enters the cold end heat exchanger where heat is added to the gas from the refrigeration load. Finally,

the gas enters the pulse-tube. In the pulse-tube, the gas shuttles back and forth in pulses rather than circulating continuously around a loop as in some refrigeration cycles. Energy is moved against a temperature gradient as work on a compliant gas volume and is rejected at the hot end heat exchanger.

1.2 Recuperative Cryocoolers

Figure 1.2 illustrates schematically a common configuration for a recuperative cryocooler, the reverse-Brayton cycle. The Joule-Thomson cryocooler is another example of a recuperative cycle. These devices share the common characteristic of having a recuperative heat exchanger that allows two continuously flowing streams at different pressures to exchange heat through a pressure boundary. The efficiency and operating temperature of a Joule-Thomson cycle is limited by the thermodynamic properties of the working fluid. An efficient reverse-Brayton cycle requires large recuperative heat exchangers and several stages of sophisticated and expensive turbines in order to achieve operating temperatures below 15 K.

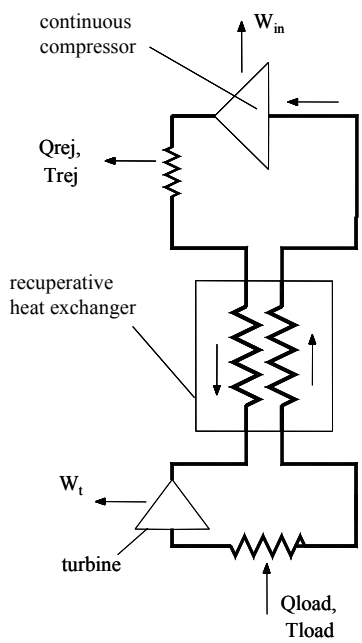

Figure 1.2: Reverse-Brayton recuperative cycle

Recuperative cycles utilize a continuous flow obtained from a centrifugal or reciprocating compressor. High-pressure fluid leaving the compressor is cooled in an aftercooler. The fluid is then pre-cooled in the recuperator by the cold fluid returning from the refrigeration load. The cold, high-pressure fluid leaving the recuperator is subsequently expanded through either a valve (Joule-Thompson cycle) or a work-extracting device (such as the turbine in a reverse-Brayton cycle) causing a temperature drop. The cold, low-pressure gas leaving the expansion device can be used to accept a refrigeration load.

1.3 Hybrid Cryocooler Configurations

The hybrid cryocooler, described in this thesis combines a regenerative upper stage with a recuperative lower stage; thereby avoiding the low temperature losses inherent in a regenerative heat exchanger yet reducing the overall temperature range that must be spanned by the recuperative cycle. This idea of a recuperative/regenerative hybrid cryocooler is not a new concept; some notable hybrid cryogenic refrigerators include the Boreas cryocooler (Crunkleton, 1993) and several Gifford-McMahon/Joule-Thomson systems (for example, Jia, 2002).

A new type of hybrid cryocooler is shown in Figure 1.3; here the regenerative stage is directly coupled to the recuperative stage via a system of check-valves and buffer volumes that rectify the oscillatory flow in the regenerative stage to provide a continuous flow that activates the recuperative stage. A single, valve-less reciprocating compressor can energize the entire system. Figure 1.3 illustrates one technique for interfacing an orifice pulse-tube (OPT) stage with a reverse-Brayton (RB) stage, referred to as the bootstrap configuration, in order to form a hybrid pulse-tube/reverse-Brayton system (Nellis, 2002).

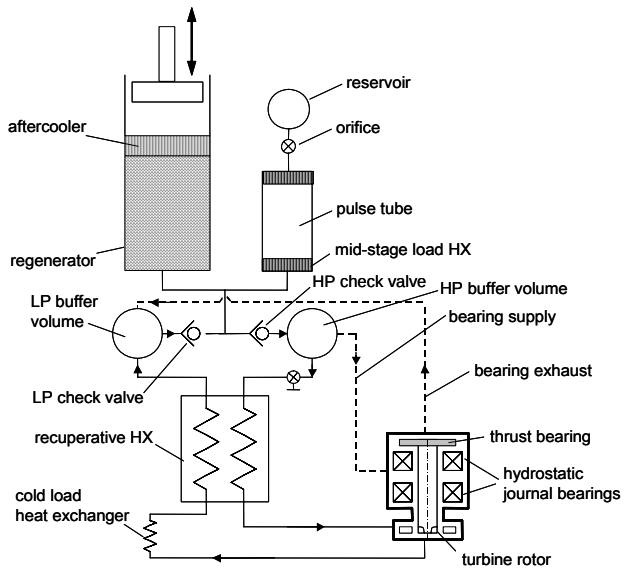

Figure 1.3: Bootstrap configuration for hybrid OPT/RB cryocooler

When the pressure in the regenerative stage goes above the pressure in the high pressure (HP) buffer volume, gas flows through the high-pressure check valve to fill the high-pressure buffer volume. When the regenerative stage pressure goes below the pressure in the low pressure (LP) buffer volume, gas flows through the low pressure check valve. Gas leaving the regenerator is therefore split into two streams. One stream flows into the pulse-tube, while the other stream charges the high-pressure buffer volume in short duration bursts. High pressure gas flows from the buffer volume in a nearly steady fashion to charge the recuperative stage. The high-pressure gas is pre-cooled by the low-pressure, colder gas in the recuperator. Then it is further cooled by expansion in the turbine.

The turbine will be rotating at very high speeds under cryogenic conditions and as such will need to be supported by gas bearings. The bearings will be thermally isolated from the turbine shaft and will be maintained at the intermediate temperature to minimize heat leak in the turbine shaft. A portion of the high pressure rectified gas is supplied to the gas bearings. This gas is used to provide support to the turbine shaft and then is returned to the low pressure buffer volume. Since this portion of the working fluid is not

expanded through the turbine and does not pick up any load yet must be processed by the compressor and regenerator, it is a direct loss for the system.

By integrating a pulse-tube system with a reverse-Brayton system, the hybrid cryocooler succeeds in combining the benefits of regenerative and recuperative cycles by operating each at its favorable operating condition. The cycle avoids the inherent losses associated with a regenerator at low temperature and also allows the reverse-Brayton stage to operate across a reasonable pressure and temperature ratio.

1.4 Motivation of Bearing Research

Future Department of Defense space-based systems will require long-life, active cryocoolers capable of achieving sub-10 K load temperatures. Currently, the available cryocooler technology at these temperatures is too massive and inefficient and in many cases, reliability is low and vibration high.

The hybrid cryocooler in the bootstrap configuration, shown in Figure 1.4 in more detail, has the potential advantages of high performance, high reliability, low mass, and simple mechanical, thermal, and electrical integration for a number of applications. One of the key aspects of the hybrid cryocooler is the cryogenic turbine and in particular the rotordynamic system used to provide support for the high speed rotating shaft. Hydrostatic gas bearings have been selected for this application because of their simplicity and ability to provide support using relatively large shaft-to-bearing clearances (relative to comparable hydrodynamic bearings), with no metal-to-metal wear. These attributes will allow the cryocooler to be manufactured at reasonable cost and operate with high reliability.

The key disadvantage of hydrostatic gas bearings is that the mass flow they consume constitutes a significant cycle penalty. A system model of this hybrid cycle has been developed and key aspects of the cycle have been verified, including the experimental demonstration of the rectifying interface at appropriate temperatures, pressures, and frequencies (Diab, 2003). The model indicates that performance of the hydrostatic gas bearings, specifically their stiffness and mass flow consumption, is critical to the overall performance of the cycle. This thesis describes work done to model the hydrostatic gas

bearings, validate the model experimentally, and develop a design procedure that allows meaningful optimization of the bearing geometry for the hybrid cryocooler application.

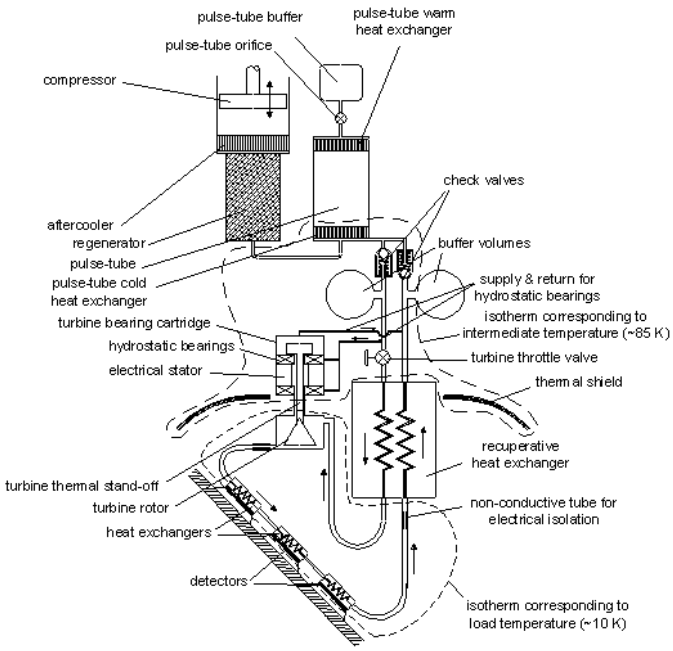

Figure 1.4: Detailed schematic of hybrid pulse-tube/reverse-Brayton system

1.5 Project Objectives

The specific technical objectives of this research were to:

- Develop fundamental modeling techniques required to design pressurized bearings for operation at cryogenic temperatures, as well as, provide valuable information on the exact nature of the tolerances involved.
- Fabricate a prototype bearing system to provide insight into the nature of the machining and assembly techniques involved.
- Test prototype bearings to measure their stiffness and mass flow consumption in order to validate the modeling effort.

CHAPTER 2

Hydrostatic Bearings

This chapter describes the operating principles of hydrostatic bearings, a fluid dynamic model of this type of bearing, and some results obtained from the model.

2.1 Description of Hydrostatic Bearings

Hydrostatic (or pressurized) gas bearings operate by exposing the surface of a shaft to high pressure gas through a series of feed holes that are arrayed circumferentially and axially as shown in Figure 2.1. The gas flowing from a feed hole loses pressure as it contracts to enter the small "curtain" or annulus formed around the feed hole diameter. This is essentially an inertial pressure loss as it is related to the acceleration of the gas. The gas subsequently flows axially outwards to the edge of the bearing through the shaft/bearing clearance and therefore loses pressure due to viscous shear.

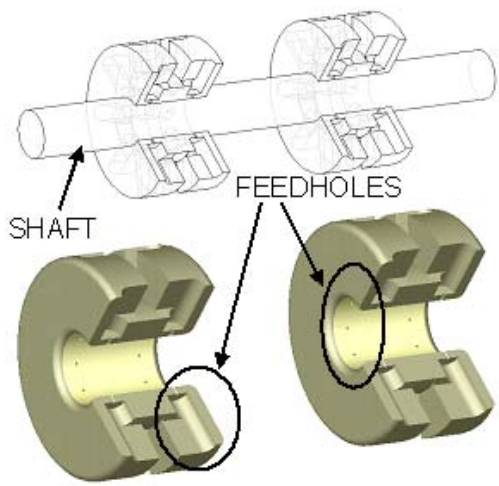

Figure 2.1: Pressurized gas bearings (double admission)

For a given mass flow rate, the inertial and viscous pressure losses described above will scale differently with the shaft-to-bearing clearance (h), roughly as $1/h$ and $1/h^3$, respectively. This relationship is shown using a resistive circuit analogy in Figure 2.2.

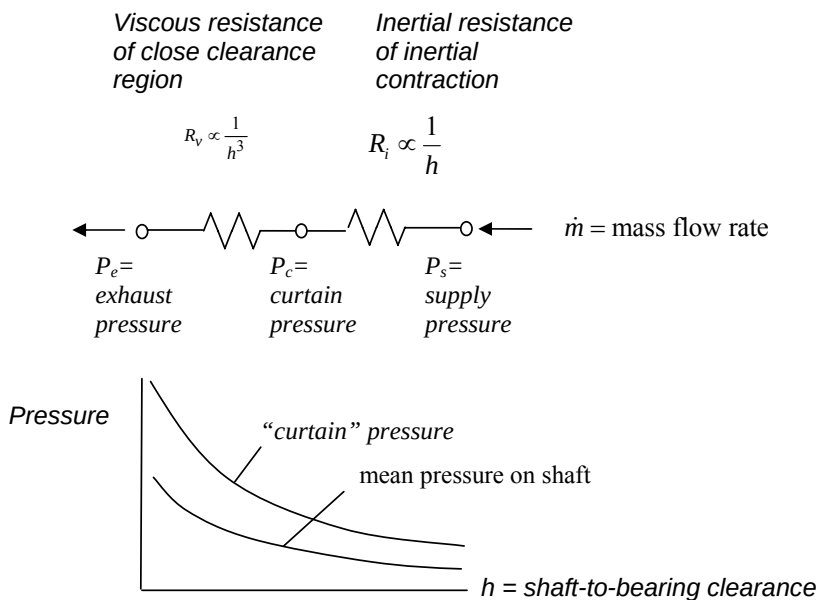

Figure 2.2: Resistive circuit analogy for hydrostatic bearings

Because the viscous pressure loss is so much more sensitive to clearance than the inertial pressure loss, any decrease in clearance will result in a dramatic increase in the curtain pressure, (P_c), the gas pressure following the inertial pressure loss. The mean pressure over the shaft surface is directly related to the curtain pressure and therefore a reduction in clearance will result in an increase in the force applied to the shaft, as shown in Figure 2.2.

In Figure 2.3, the operation of the bearing is depicted schematically. Case 1 shows a centered shaft, while in Case 2 the shaft is off-center. The supply and exhaust pressures are fixed and assumed to be equal in both of the cases. In Case 1, the clearances at locations diametrally opposite one another, a and b in Figure 2.3, are identical. The viscous resistance at a is equal to the viscous resistance at b and the inertial resistance at a is equal to the inertial resistance at b. If the shaft is now perturbed from its centered position, as shown in Case 2, the clearance at location b becomes less than the centered clearance and the clearance at location a becomes greater. This causes the viscous resistance associated with the clearance gap at b to increase relative to the inertial resistance. The viscous resistance associated with the clearance gap at location a

decreases relative to the inertial resistance. The net result is a larger curtain pressure at location b compared to location a, which produces a net, pressure induced force on the shaft that tends to return it to its centered position. The net result of considering all of the feed holes arrayed around a shaft gives the bearing an effective stiffness.

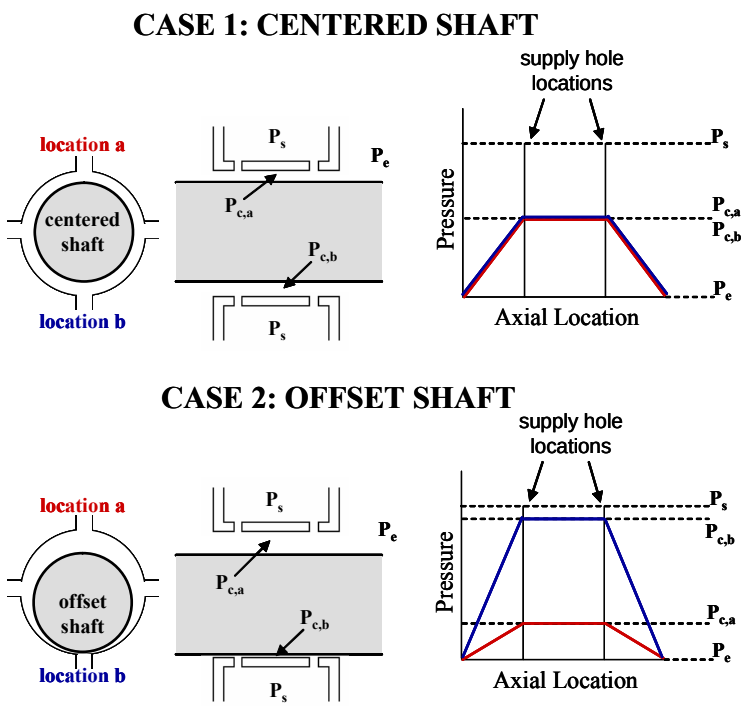

Figure 2.3: Hydrostatic bearing schematic

2.2 Hydrostatic Bearing Model

The nomenclature used throughout this section and in the bearing model is summarized below.

A	surface area of curtain (m^2)
a_s	width of slot (m)
b	axial length of bearing (m)
c	centered radial clearance (m)
cf	stiffness correction factor

C_D	discharge coefficient
C_k	stiffness scaling parameter
C_m	mass flow rate scaling parameter
F_n	normal force (N)
f_n	natural frequency (Hz)
h	height of equivalent slot (m)
k	total stiffness of bearing (N/m)
L	axial extent of equivalent slot (m)
L/b	station, nondimensional location of supply holes
$\dot{m}$	total mass flow rate consumed (kg/s)
$\dot{m}_{slot}$	mass flow rate through equivalent slot (kg/s)
m_{shaft}	mass of shaft (kg)
N	number of feed holes per ring
P_c	curtain pressure (Pa)
P_e	exhaust pressure (Pa)
P_s	supply pressure (Pa)
$\bar{P}_v$	mean viscous pressure over shaft (Pa)
R	ideal gas constant (J/kg-K)
r_h	supply hole radius (m)
r_s	shaft radius (m)
T	gas temperature (K)
W	bearing pressure factor

greek symbols

$\Delta\bar{p}$	mean pressure elevation over shaft (Pa)
ε	ratio of offset between shaft and bearing centerlines to centered clearance
μ	viscosity of gas (kg/m-s)
γ	ratio of specific heats
ρ	local density of gas (kg/m^3)
θ	angle between load line and feedhole (rad)

subscripts

i i'th feedhole/slot

The hydrostatic bearing model described in this section was implemented in the *Engineering Equation Solver* (*EES*) software (Klein, 2003). The *EES* software was used because of its ability to parametrically study and optimize bearing parameters. *EES* also has built-in property functions for most common gases over a large range of temperatures and pressures. Bearing geometry and operating conditions can be input into the model and are schematically shown in Figure 2.4. The model can then predict the performance of a hydrostatic bearing, in particular stiffness and mass flow consumption. A flow chart of the model calculations is shown in Figure 2.5. These calculations will be described in more detail in this section.

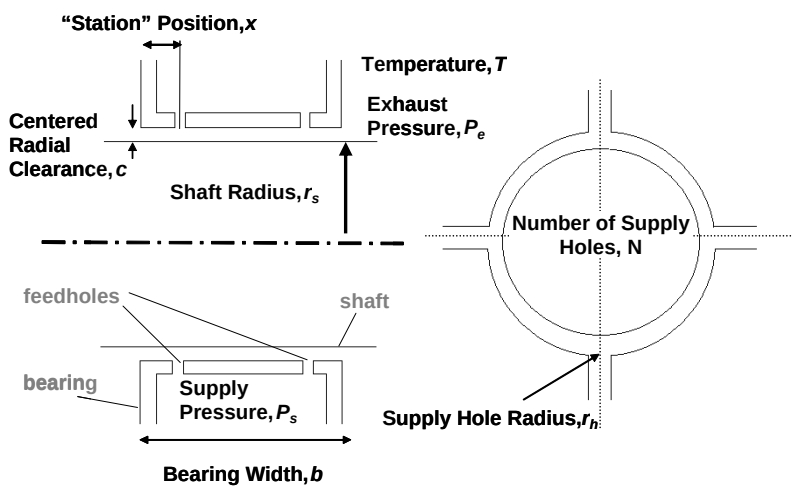

Figure 2.4: Hydrostatic bearing model inputs for EES

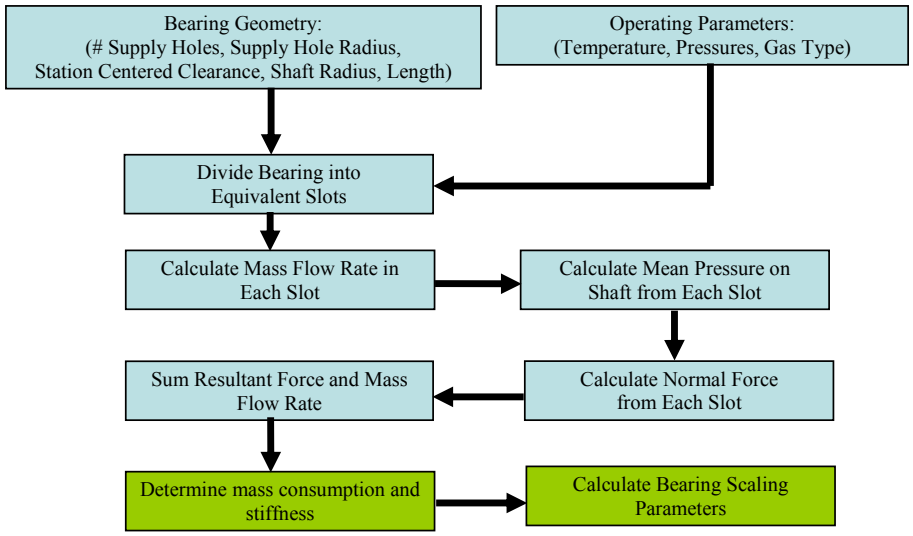

Figure 2.5: Hydrostatic bearing model flowchart

The bearing model developed in this work uses the equivalent slot concept, proposed by Shires (1964). The equivalent slot concept is illustrated schematically in Figure 2.6.

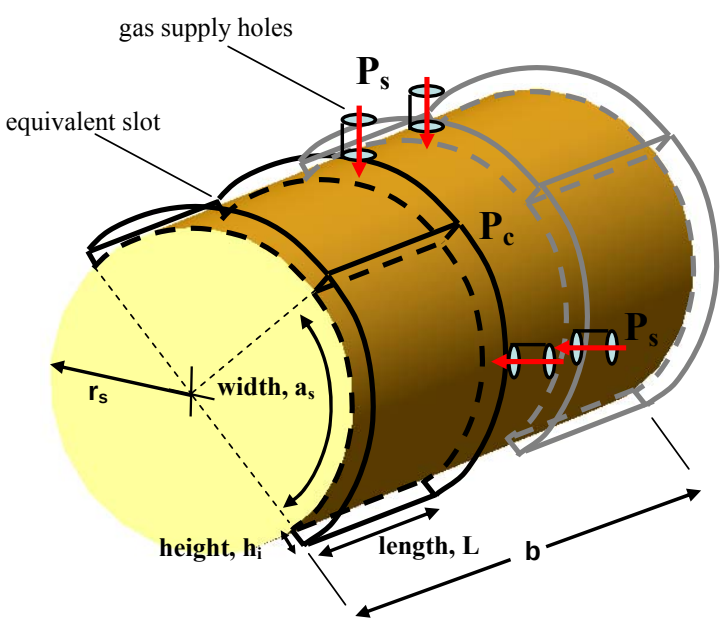

Figure 2.6: Equivalent slot concept for a hydrostatic bearing

The bearing is essentially unrolled and the flow from each feed hole is assumed to move axially through a "slot" and exit at the bearing edge. The width of each slot perpendicular to the flow (a_s) is taken to be twice the perimeter of the bearing in order to account for symmetry (that is, an assumed equal amount of flow goes to each edge of the bearing) divided by the number of feed holes that are circumferentially arrayed about the shaft ($a_s = 4\ \pi r_s/N$). The height of each slot (h_i) depends on the position of the shaft center relative to the bearing center, as shown in Figure 2.7 (Powell, 1970), and is computed according to Eq. (1).

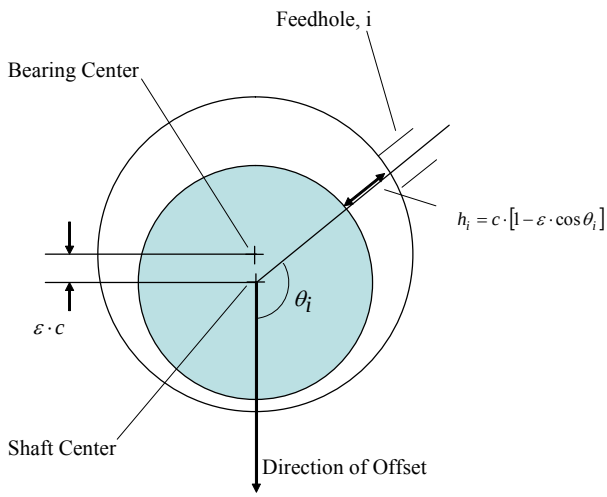

Figure 2.7: Slot height dependence on shaft/bearing centers

$$h_i = c \cdot \left[1 - \varepsilon \cdot \cos\left(\theta_i\right)\right] \text{ where } \theta_i = \frac{2 \cdot i - 1}{N} \cdot \pi \text{ for } i = 1..\frac{N}{2} \qquad (1)$$

where c is the centered shaft/bearing clearance and ε is the ratio of the offset between the shaft and bearing centerlines and the centered clearance. Equation (1) implies that the direction of the shaft perturbation is midway between two feed holes and is only valid when the bearing has an even number of feed holes. Laminar, fully-developed flow is

assumed in the slot, leading to the following relationship between the mass flow rate through the slot ($\dot{m}_{slot,i}$) and the pressure gradient (*dp/dx*) (Munson, 1998):

$$\frac{dp}{dx} = \frac{-12 \cdot \mu}{a_s \cdot \rho \cdot h_i^3} \cdot \dot{m}_{slot,i} \tag{2}$$

where μ is the viscosity and ρ is the local gas density. The gas is assumed to be isothermal (at temperature *T*, the entering gas temperature) with constant viscosity and to obey the ideal gas law with gas constant *R*. Substituting the ideal gas law for density and integrating Eq. (2) from the "curtain" pressure ($P_{c,i}$) to the exhaust pressure (p_e) leads to:

$$p_{c,i}^2 - p_e^2 = \frac{24 \cdot \mu \cdot \dot{m}_{slot,i} \cdot R \cdot T \cdot L}{a_s \cdot h_i^3} \tag{3}$$

where *L* is the axial distance from the feed hole to the edge of the bearing. The mass flow rate through each "curtain" area is related to the supply pressure (p_s) and the curtain pressure using equations for compressible flow (Fay, 1994):

$$\dot{m}_{slot,i} = \begin{cases} \dfrac{C_D \cdot p_s \cdot A_i}{R \cdot T} \cdot \sqrt{2 \cdot R \cdot T} \cdot \sqrt{\left(\dfrac{\gamma}{\gamma - 1}\right) \cdot \left(\left(\dfrac{p_{c,i}}{p_s}\right)^{2/\gamma} - \left(\dfrac{p_{c,i}}{p_s}\right)^{\gamma+1/\gamma}\right)} \\ \qquad \text{for } \dfrac{p_{c,i}}{p_s} \geq \left(\dfrac{2}{\gamma + 1}\right)^{\gamma/\gamma-1} \\ \dfrac{C_D \cdot p_s \cdot A_i}{R \cdot T} \cdot \sqrt{2 \cdot R \cdot T} \cdot \sqrt{\left(\dfrac{\gamma}{\gamma - 1}\right) \cdot \left(\left(\dfrac{2}{\gamma + 1}\right)^{2/\gamma-1} - \left(\dfrac{2}{\gamma + 1}\right)^{\gamma+1/\gamma-1}\right)} \\ \qquad \text{for } \dfrac{p_{c,i}}{p_s} < \left(\dfrac{2}{\gamma + 1}\right)^{\gamma/\gamma-1} \end{cases} \tag{4}$$

where C_D is the discharge coefficient (taken to be 1.0) and A_i is the area of the curtain. For an inherently compensated journal bearing, the curtain area is approximately equal to the annular section formed between the perimeter of the feed hole and the shaft, ($2\pi r_h h_i$).

Equations (3) and (4) together allow for the solution of the mass flow rate and curtain pressure for each slot. Note that this is true for both single and double admission bearings. For double admission bearings only ½ of the supply hole is active.

The mean pressure elevation (relative to the exhaust pressure) seen by the shaft surface at each feed hole ($\Delta\overline{p}_i$) can be evaluated by integrating equation (2) from the bearing edge to the feedhole. A constant curtain pressure between feed holes is assumed. The result is:

$$\Delta\overline{p}_i = \frac{2\cdot L\cdot\left(\overline{p}_{v,i} - p_e\right) + \left(b - 2\cdot L\right)\cdot\left(p_{c,i} - p_e\right)}{b}$$

where (5)

$$\overline{p}_{v,i} = \frac{a_s\cdot h_i^3\cdot\left(p_{c,i}^3 - p_e^3\right)}{36\cdot\mu\cdot\dot{m}_{slot,i}\cdot R\cdot T\cdot L}$$

and b is the axial length of the bearing. The normal force on the shaft from the i'th feedhole ($F_{n,i}$ – the force directly opposing the shaft displacement) is obtained by carrying out the integration shown in Equation (6):

$$\begin{aligned} F_{n,i} &= \int_{\theta_i-\frac{\pi}{N}}^{\theta_i+\frac{\pi}{N}} \Delta\overline{p}_i\cdot b\cdot r_s\cdot\cos\left(\theta\right)\cdot d\theta \\ &= \Delta\overline{p}_i\cdot b\cdot r_s\cdot\left[\sin\left(\theta_i+\frac{\pi}{N}\right) - \sin\left(\theta_i-\frac{\pi}{N}\right)\right] \end{aligned} \tag{6}$$

The normal stiffness exhibited by the bearing (k) is the ratio of the net normal force imposed on the shaft to its radial displacement. The stiffness and the total mass flow rate consumed by the bearing ($\dot{m}$) are obtained by summing the contributions of the individual feed holes.

$$k = cf\cdot\frac{\sum_{i=1}^{N} F_{n,i}}{\varepsilon\cdot c} \tag{7}$$

$$\dot{m} = \sum_{i=1}^{N} \dot{m}_{slot,i} \tag{8}$$

where *cf* is a correction factor (dimensionless number less than unity) meant to account for the circumferential interaction between adjacent feedholes - an effect that is otherwise neglected by this model.

To facilitate design and optimization studies using the hybrid cryocooler system model, two scaling laws are developed to allow the approximate prediction of mass flow rate and stiffness given particular operating conditions and geometry:

$$\dot{m} = C_m \cdot \frac{p_e \cdot c^3 \cdot \left(p_s - p_e\right)}{R \cdot T \cdot \mu} \tag{9}$$

$$k = C_k \cdot \frac{\left(p_s - p_e\right) \cdot \left(2 \cdot r_s\right)^2}{c} \tag{10}$$

where C_m and C_k are scaling parameters related to mass flow consumption and stiffness, respectively. The primary purpose of the model and the experimental measurements is to predict and then verify the values of C_m and C_k that can be achieved by an optimally designed bearing in order to allow a realistic assessment of the potential performance of the hybrid refrigeration cycle described in Chapter 1.

Several mathematical checks of the model were conducted with a centered bearing (ε approaching 0). These checks included verifying that the centered clearances for each equivalent slot were equal, verifying that the summation of restoring forces ($F_{n,i}$) for all equivalent slots was zero, and verifying that the curtain pressures ($P_{c,i}$) for all equivalent slots were equal.

The predicted results were also compared to values reported for similar models described in the literature. Figure 2.8 shows the variation of the stiffness scaling parameter, C_k, as a function of the ratio of the pressure drop in the bearing clearance to

the total pressure drop when the bearing is centered. This value is called the bearing pressure factor, and is quantified as follows:

$$\text{Bearing Pressure Factor, } W = \frac{P_{c,centered} - P_e}{P_s - P_e} \qquad (11)$$

The lines in Figure 2.8 are generated by the model assuming a quarter station bearing geometry (i.e., $L/b = 0.25$) with 8 supply holes/ring and an aspect ratio (i.e., $b/2\ r_s$) of 1.5. The points were taken from previous published literature (Shires, 1964; Powell 1970) for a bearing with 8 supply holes/ring and an aspect ratio approaching 0. The discrepancies can be accounted for by the difference in aspect ratios. The agreement is relatively good otherwise.

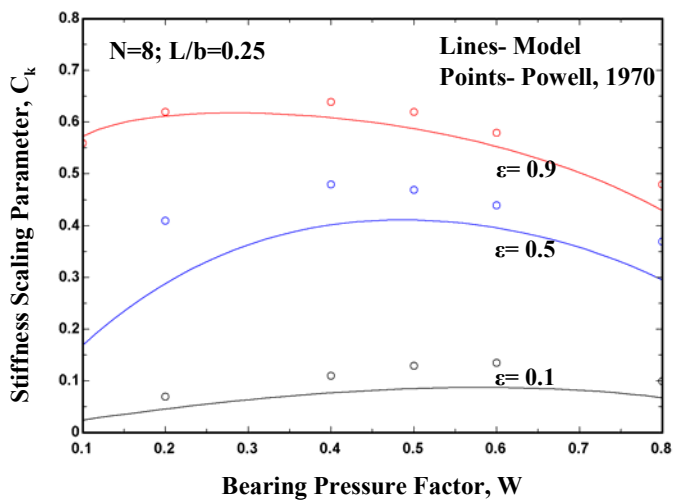

Figure 2.8: Stiffness scaling parameter vs. bearing pressure factor

2.3 Model Results with Air

This section describes the results of exercising the model using air as a working fluid. The model is used to obtain a realistic and producible design for a prototype set of bearings. The nominal shaft radius (r_s) and bearing width (b) were set by manufacturing requirements. In order to maintain a reasonable tolerance over a bore, the aspect ratio of

the hole must be kept below about 1.5. This means that if a shaft diameter of 0.2" is specified then the bore for the inner bearing diameter cannot exceed about 0.3".

This leaves 3 bearing geometric parameters that must be specified to complete the design:

- Supply hole location, or station (L/b)
- Number of supply holes (N)
- Radius of supply holes (r_h)

2.3.1 Effect of Station Location

The model was used to study the effect of supply hole radius and supply hole location on bearing performance. The results of this study are shown in Figures 2.9, 2.10, and 2.11 for an inherently compensated journal bearing with 8 feedholes per supply hole ring operating with air at room temperature with a pressure ratio (supply-to-exhaust) of 1.2. The nominal shaft radius (r_s) was set to 0.100 inch (2.55 mm), the total width of the bearing (b) was set to 0.313 inch (8.0 mm) and the shaft/bearing radial clearance (c) was set to 0.002 inch (50 μm) based on achievable manufacturing tolerances. The smallest achievable supply hole radius using standard machining methods such as electric-discharge-machining (EDM) was found to be 0.004 inches (.102 mm). This enforces a practical lower limit on the supply hole radius.

Figure 2.9 shows how the bearing mass flow rate varies with the supply hole radius as the station (L/b) is varied. A station of 0.1 means that there are 2 rows of supply holes placed very close to each edge of the bearing while a station of 0.5 means that a single row of supply holes are placed at the center of the bearing. It can be seen that a station of 0.5 produces the minimum mass flow consumption for all supply hole radii and the mass flow rate increases with increasing supply hole radius. At a fixed supply hole radius the viscous and inertial pressure drops will not necessarily be balanced. When the supply hole radius is small it can be seen that the inertial pressure loss has minimal effect on the mass flow rate and the lines of constant station seem to converge. Conversely, at larger supply hole radii (greater than ~0.005") the inertial pressure loss will have a larger effect on the mass flow rate and will decrease with increasing station. Increasing the length of the equivalent slot (L) by increasing the station (L/b) will cause the curtain pressure to

increase (i.e. the viscous pressure drop increases relative to the inertial pressure drop). This will decrease the mass flow rate in the equivalent slot ($\dot{m}_{slot,i}$) as can be seen from Equation (4).

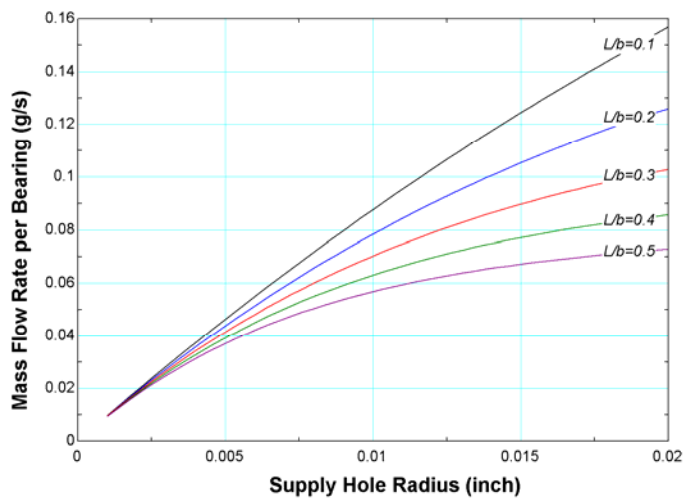

Figure 2.9: $\dot{m}$ vs. r_h using air for various station

Figure 2.10 shows how the bearing stiffness varies with the supply hole radius as the location of the supply holes is varied. It can be seen that there is an optimal supply hole radius associated with maximizing the bearing's stiffness for each station position. Also, at this optimal supply hole radius, the smallest value of the station (0.1 in Figure 2.10) will produce the highest stiffness while a station of 0.5 will produce the lowest stiffness at the optimal supply hole radius. This occurs because at the optimal supply hole radius the viscous and inertial pressure drops are balanced (each is approximately ½ the overall pressure drop), and the curtain pressure ($P_{c,i}$) is constant for all stations. Since the curtain pressure is constant the mean pressure seen by the shaft surface at each feedhole ($\Delta\overline{p}_i$) must increase as the length of the equivalent slot decreases (i.e. the curtain pressure will act over a larger portion of the shaft). An increase in the mean pressure seen by the shaft

surface will result in an increase in the normal force on the shaft as can be seen from Equation (6).

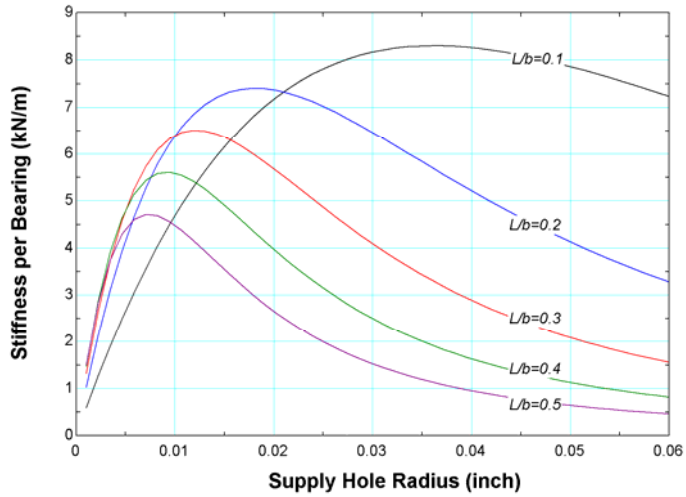

Figure 2.10: k vs. r_h using air for varying station

Figure 2.11 shows how the ratio of stiffness to mass consumption varies with supply hole radius for different station positions. The hybrid cryogenic refrigeration cycle described earlier requires a bearing with high stiffness and low mass flow consumption. To first order, this suggests that the ratio, $k/\dot{m}$, should be maximized. It can be seen that $k/\dot{m}$ is maximized with a station of 0.5. In a typical hydrostatic bearing application, the stiffness is the most important parameter and mass flow consumption is of secondary importance. Thus many hydrostatic bearings are double-admission (i.e., have a station that is less than 0.5). Figure 2.11 illustrates that single-admission bearings (i.e., bearings with a station = 0.5) may be more suitable for a cryogenic turbomachine. More complete optimization using the hybrid cryocooler system model is required to draw this conclusion.

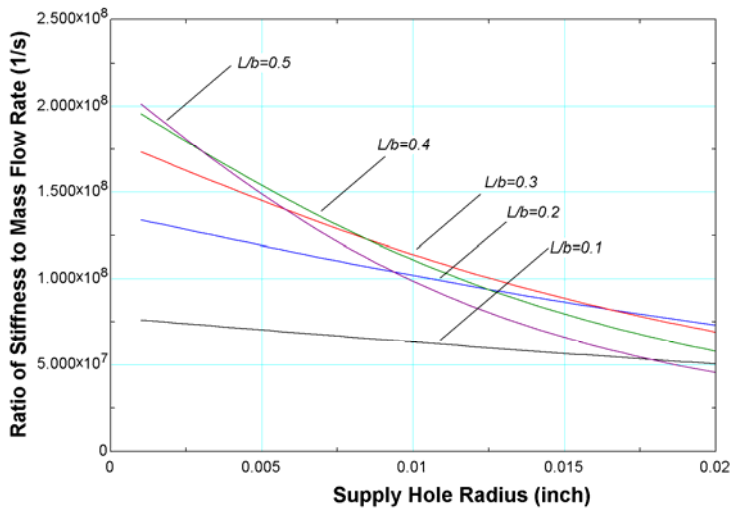

Figure 2.11: $k/\dot{m}$ vs. r_h using air for varying Station

2.3.2 Effect of Number of Supply Holes

The model was used to study the effect of the number of supply holes on bearing performance. This study is shown in Figures 2.12, 2.13, and 2.14 for a 0.5 station (i.e., single-admission) inherently compensated journal bearing operating with air at room temperature and at a pressure ratio of 1.2 (supply-to-exhaust). The nominal shaft radius (r_s) is set to 0.100 inch (2.54 mm), the total width of the bearing (b) is set to 0.313 inch (8.0 mm) and the shaft/bearing radial clearance (c) is set to 0.002 inch (50 μm).

Figure 2.12 shows how the bearing mass flow rate varies with the supply hole radius as the number of supply holes per ring (N) is varied. It can be seen that 6 supply holes produces the minimum mass flow consumption for all supply hole radii while 14 supply holes produces the maximum. Also, points of maximum stiffness occur at the same mass flow rate for all numbers of supply holes, but the required supply hole radius for maximum stiffness decreases as the number of supply holes increases.

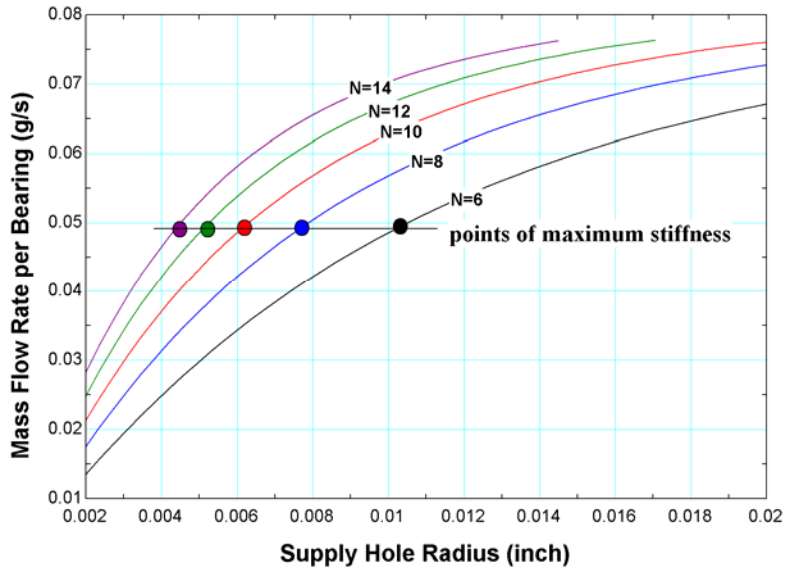

Figure 2.12: $\dot{m}$ vs. r_h using air for varying number of supply holes

Figure 2.13 shows how the bearing stiffness varies with the supply hole radius as the number of supply holes is varied. It can be seen that there is an optimal supply hole radius associated with maximizing the bearing's stiffness for each number of supply holes. Also, at this optimal supply hole radius, 14 supply holes will produce the highest stiffness while 6 supply holes will produce the lowest stiffness; but the difference between the highest and lowest stiffness is marginal.

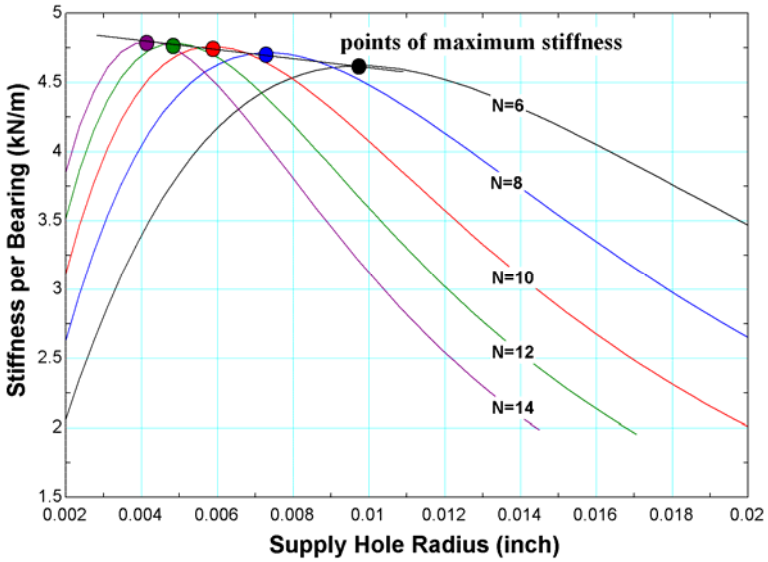

Figure 2.13: k vs. r_h using air for varying number of supply holes

Figure 2.14 shows how the ratio of stiffness to mass consumption varies with supply hole radius for different number of supply holes. As already stated, the hybrid refrigeration cycle requires a bearing of high stiffness and low mass flow consumption. To first order, this suggests that the ratio, $k/\dot{m}$ should be maximized and it can be seen that $k/\dot{m}$ is maximized with 6 supply holes. Also, points of maximum stiffness occur at the same $k/\dot{m}$ for each number of supply holes, but at decreasing supply hole radius for an increasing number of supply holes.

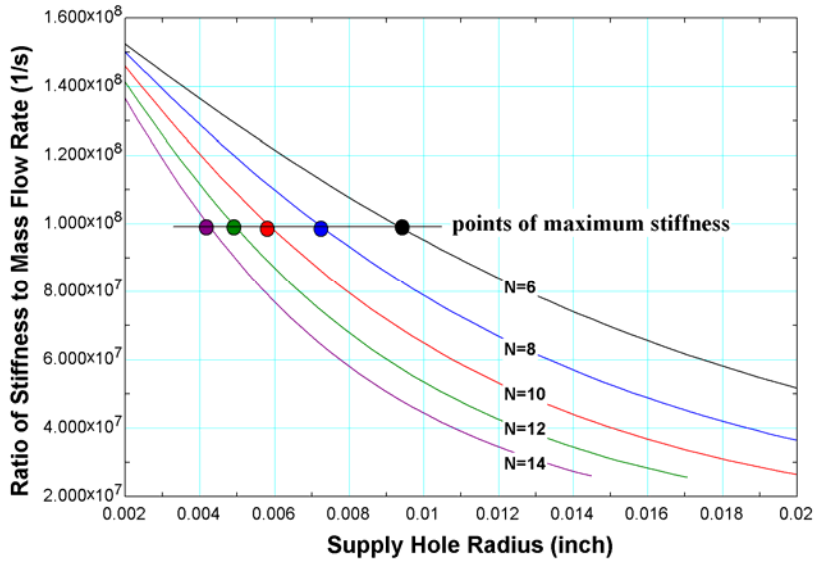

Figure 2.14: $k/\dot{m}$ vs. r_h using air for varying number of supply holes

This investigation again shows that a trade off exists between stiffness and mass flow consumption for the single admission bearing. A bearing with 6 supply holes will always consume less mass flow than a bearing with more supply holes. The stiffness of a bearing with 6 supply holes will be slightly less that other designs with more supply holes, but this may be less important for a cryogenic turbomachine than for other applications. Fewer than 6 supply holes will result in large oscillations in stiffness seen by the shaft during an orbit with may generate unanticipated rotordynamic problems.

2.3.3 Effect of Supply Hole Radius

Both the mass flow consumption and stiffness of the bearing are effected by the supply hole radius. The mass flow consumption varies proportionately to the supply hole radius and an optimal supply hole radius that maximizes stiffness can be determined. This optimal supply hole radius may occur at a prohibitively high mass flow consumption. Therefore, the mass flow consumption can be greatly reduced, at the cost of slightly reducing the stiffness by manufacturing a bearing with a smaller than optimal supply hole radius. This effect is illustrated in Figure 2.15 which shows both stiffness and mass flow consumption for a bearing with 8 supply holes that has the geometry and

operating conditions described in section 2.3.2. Decreasing the supply hole radius to 0.004" from 0.00725 (the optimal supply hole radius shown in Figure 2.15) decreases the stiffness by about 14% and decreases the mass flow consumption by about 35%.

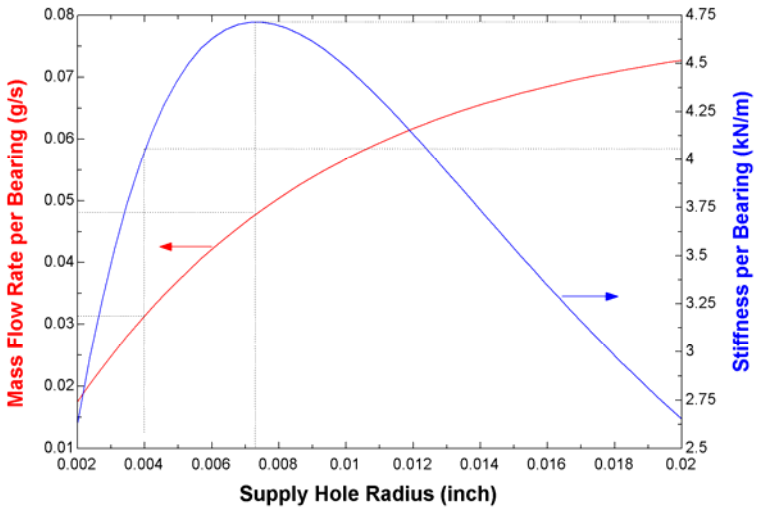

Figure 2.15: Effect of non-optimized r_h using Air (N=8)

2.4 Model Results with Helium

The effect of using cryogenic, high pressure, helium gas (rather than air near ambient pressure at room temp) on bearing performance and geometry was investigated. The following parameters were studied:

- Supply hole location, or station (L/b)
- Number of supply holes (N)
- Radius of supply holes (r_h)

2.4.1 Effect of Station Location

The model was used to study the effect of supply hole radius and supply hole location on bearing performance, similar to the study described section 2.3.1. The results are shown in Figures 2.16, 2.17, and 2.18 for an inherently compensated journal bearing with 8 feedholes per ring that is operating with helium at 60 K between 175 and 120 psig (1.2 and .8 MPa); a pressure ratio of 1.4. These conditions are nominally consistent with

those expected in the hybrid cryocooler. The nominal shaft radius (r_s) is set to 0.100 inch (2.54 mm), the total width of the bearing (b) is set to 0.313 inch (8.0 mm) and the shaft/bearing radial clearance (c) is set to 0.0005 inch (13 μm). Note that the much lower clearance is absolutely essential to the successful operation of the hybrid cycle, as will be explored in the optimization section of this thesis.

Figure 2.16 shows how the bearing mass flow rate varies with the supply hole radius as the location of the supply holes is varied. As shown previously for air, a station of 0.5 produces the minimum mass flow consumption for all supply hole radii when operating at cryogenic conditions.

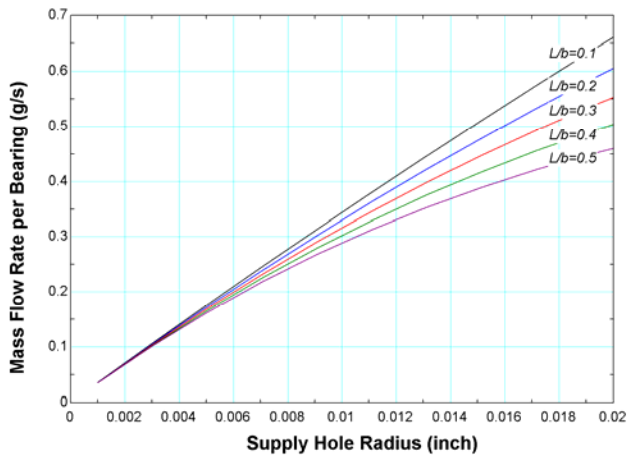

Figure 2.16: $\dot{m}$ vs. r_h using cryogenic helium for varying station

Figure 2.17 shows how the bearing stiffness varies with the supply hole radius as the location of the supply holes is varied. Again, it can be seen that there is an optimal supply hole radius associated with maximizing the bearing's stiffness for each station position. At the optimal supply hole radius, a station of 0.5 will produce the lowest stiffness.

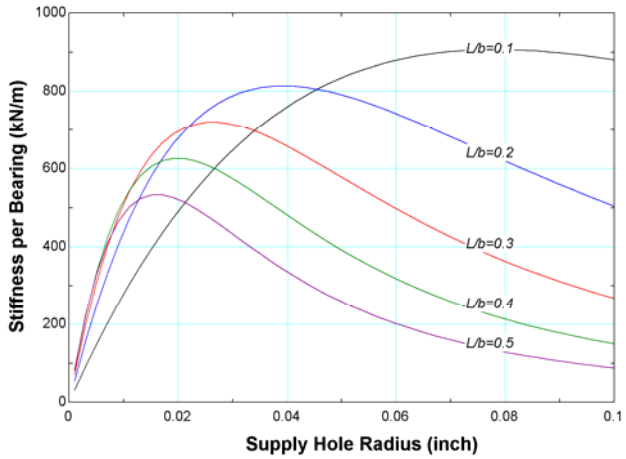

Figure 2.17: k vs. r_h using cryogenic helium for varying station

Figure 2.18 shows how the ratio of stiffness to mass flow consumption varies with supply hole radius for different station positions. As shown in section 2.3.1, the ratio of stiffness to mass flow consumption should be maximized to meet the requirements of a cryogenic refrigeration cycle. Again, $k/\dot{m}$ is maximized with a station of 0.5 for small supply hole radii.

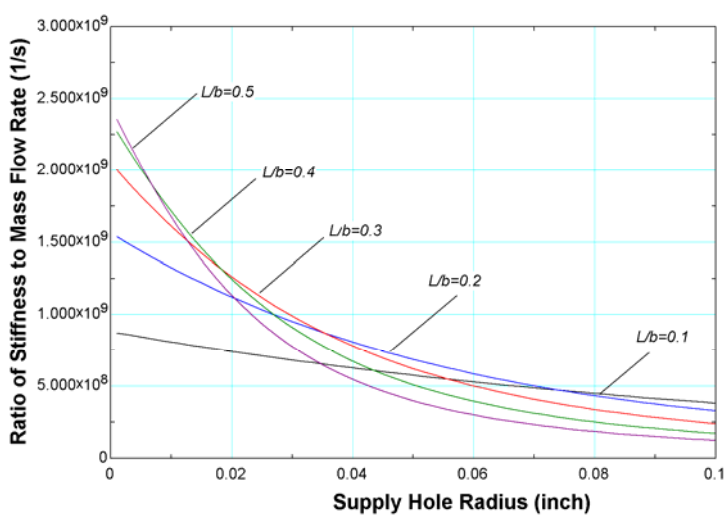

Figure 2.18: $k/\dot{m}$ vs. r_h using cryogenic helium for varying station

The general trends seen for bearing operating with air near ambient pressure at room temperature hold for operation with cryogenic, high pressure helium. However, in general, the higher mass flow rate is due mostly to a larger pressure ratio across the bearing. This larger mass flow rate, coupled to the operating temperature, pressures, and gas properties cause an increase in the mean pressure elevation seen by the shaft surface at each feed hole ($\Delta\overline{p}_i$) according to Equation (5). The increased mean pressure elevation seen by the shaft surface will increase the normal force on the shaft from the feedhole ($F_{n,i}$) according to Equation (6).

2.4.2 Effect of Number of Supply Holes

The model was used to study the effect of the number of supply holes on bearing performance. This study is shown in Figures 2.19, 2.20, and 2.21 for a 0.5 station inherently compensated journal bearing with 8 feedholes that is operating with helium at 60 K between 175 and 120 psig (1.2 and 0.8MPa); a pressure ratio of 1.4. The nominal shaft radius (r_s) is set to 0.100 inch (2.55 mm), the total width of the bearing (b) is set to 0.313 inch (8.0 mm) and the shaft/bearing radial clearance (c) is set to 0.0005 inch (13 μm).

Figures 2.19, 2.20, and 2.21 show trends that are similar to the corresponding figures generated with air (i.e., Figures 2.12, 2.13, and 2.14 in section 2.3.2). However, points of maximum stiffness occur at higher mass flow rates using high pressure helium at cryogenic conditions. Likewise, the optimal supply hole radii are larger for any number of supply holes. As previously mentioned, the optimal supply hole radius is the radius for the given supply hole location and number of supply holes that balances the inertial and viscous pressure losses through the bearing. Since larger mass flow rates are required when operating with high pressure, cryogenic helium, larger supply hole radii will result in the balance of the inertial and viscous pressure losses.

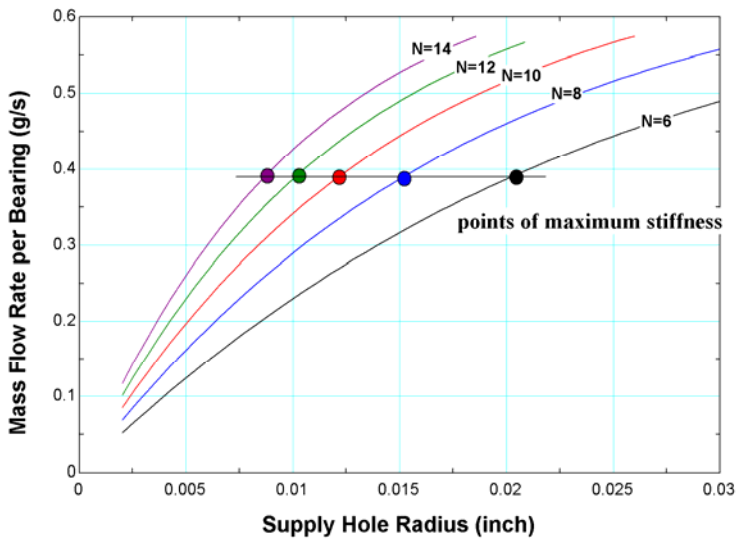

Figure 2.19: $\dot{m}$ vs. r_h using cryogenic helium for varying number of feed holes

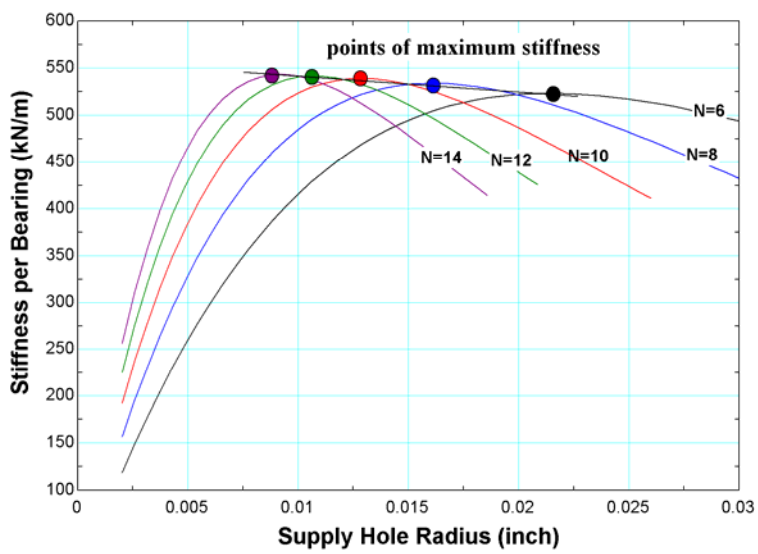

Figure 2.20: k vs. r_h using cryogenic helium for varying number of supply holes

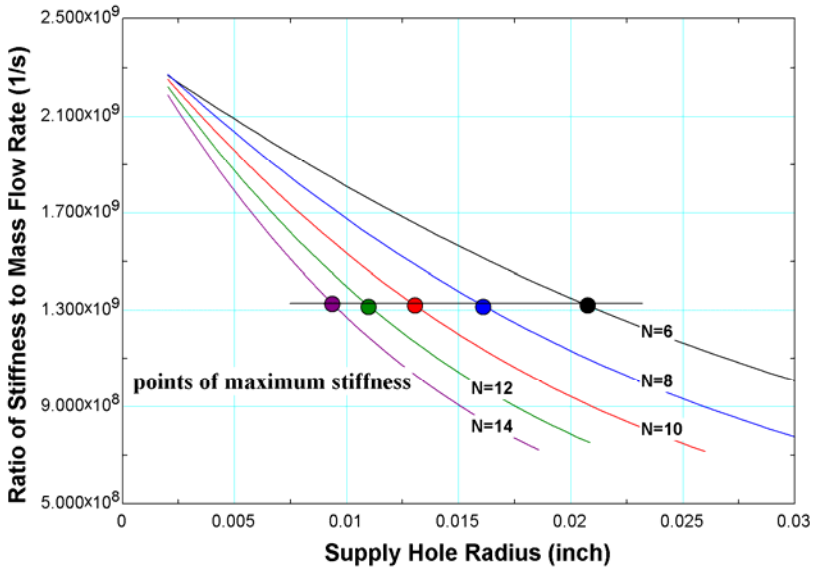

Figure 2.21: $k/\dot{m}$ vs. r_h using cryogenic helium for varying number of supply holes

2.4.3 Effect of Supply Hole Radius

The mass flow consumption can be greatly reduced, at the cost of slightly reducing the stiffness, by manufacturing a bearing with a smaller than optimal supply hole radius (a similar trend was observed when operating with air in section 2.3.3). This effect is illustrated in Figure 2.22, which shows both stiffness and mass flow consumption for a bearing with 8 supply holes with the geometry and conditions described in section 2.4.2. The radius of the supply hole is a very important parameter, as decreasing the supply hole radius from 0.016" to 0.004" decreases the stiffness by about 47% and decreases the mass flow consumption by about 65%.

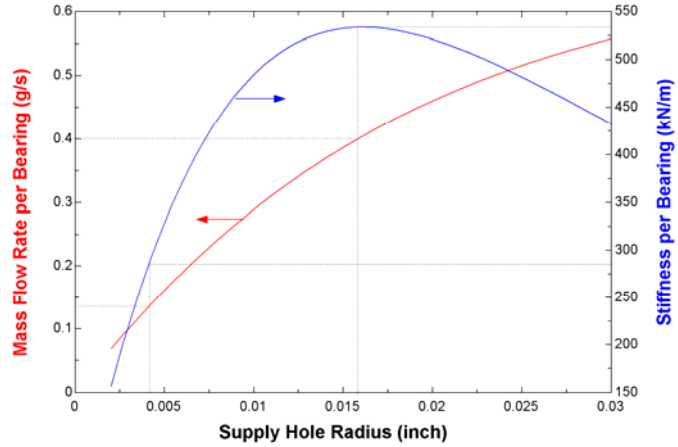

Figure 2.22: Effect of non-optimized r_h using cryogenic helium (N=8)

2.5 Comparison of Required Clearances

The model was used to compare the required clearance for a bearing with 8 supply holes and a supply hole radius of 0.004" with otherwise the same geometry described in section 2.4.2. Results are shown both for a bearing operating with air at room temperature and low pressure and helium at cryogenic temperature and high pressures. Figure 2.23 shows that a much smaller shaft/bearing clearance is required to maintain a reasonable mass flow rate when operating with helium at 60 K and high pressures. Figure 2.24 shows that the stiffness is much higher when operating with helium at 60 K and high pressures. Cryocooler design should be focused on minimizing the shaft-bearing clearance as this will reduce the mass flow consumption while increasing the stiffness of the bearings, which will result in increased overall cycle performance.

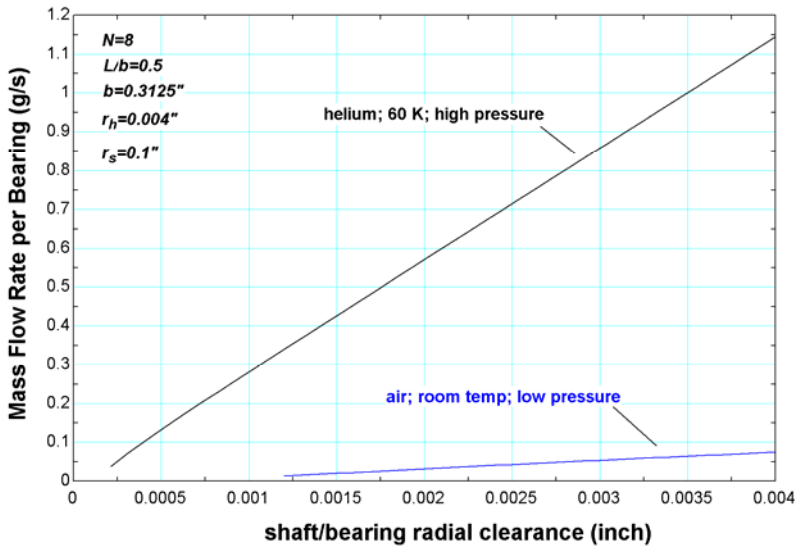

Figure 2.23: Mass flow rate vs. radial clearance comparison

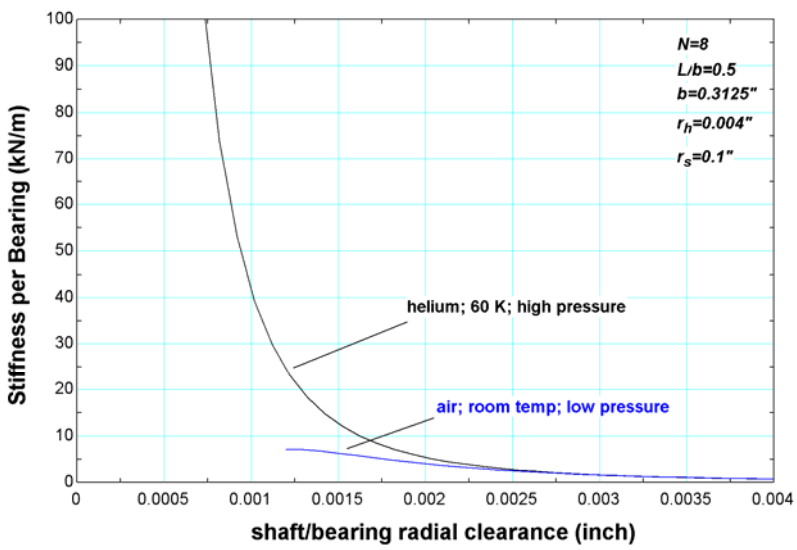

Figure 2.24: Stiffness vs. radial clearance comparison

2.6 Prototype Bearing Design Summary

Sections 2.3 and 2.4 showed that a trade-off exists between stiffness and mass flow consumption for both bearings operating at any conditions; specific investigations were shown for bearings operating with air at room temperature and low pressures and bearings operating with helium at cryogenic temperatures and high pressures. A bearing with a station of 0.5 (single admission, i.e. 1 ring of supply holes) was shown to always consume less mass flow than a bearing with a smaller station. The stiffness of the single admission bearing will be less that other designs at large supply hole radii and the maximum possible stiffness will be less than dual admission bearings. However, $k/\dot{m}$ is highest for a single admission bearing at small supply hole radii. This ratio is particularly relevant to the performance of the hybrid cryocooler cycle and therefore, in the absence of the more thorough optimization that will follow, the test bearings were built with a single admission design.

Two hydrostatic journal bearings were built and tested as part of this project. These bearings were optimized for use with air using the hydrostatic bearing model. The journal bearings are of identical design: single admission (L/b=0.5), inherently compensated hydrostatic bearings with 8 feedholes each with radius (r_h) of 0.004 inch (0.1 mm). The nominal shaft radius (r_s) is 0.100 inch (2.55 mm), the total width of the bearing (b) is 0.313 inch (8.0 mm) and the shaft/bearing radial clearance (c) is 0.002 inch ± 0.0005 inch (50 μm ± 12 μm). A drawing of the journal bearing design is shown in Figure 2.25.

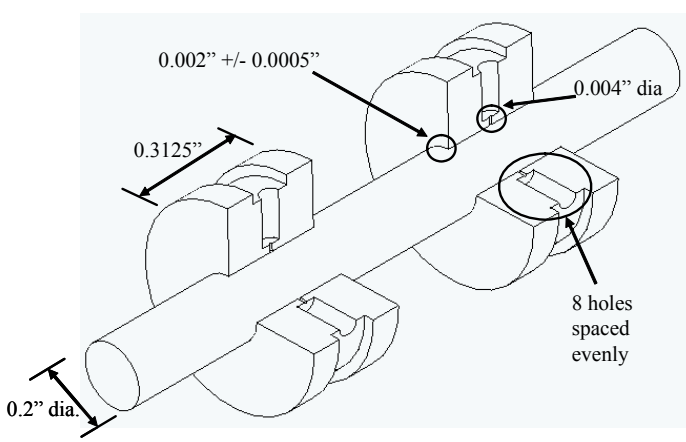

Figure 2.25: Prototype bearing design sketch

CHAPTER 3

Fabrication of a Rotordynamic System

This chapter describes the steps taken to design and build a test facility for the hydrostatic bearings.

3.1 Test Fixture

In order to validate and refine the hydrostatic gas bearing model, an experimental test facility was designed and fabricated. The facility contains the two journal bearings, a shaft (*Vermont Gage* class X-minus plug gages with a tolerance of +0.00000", -0.00004"), a pneumatic drive system, and a thrust bearing. A cutaway drawing of the test facility and photographs of the test facility are shown in Figure 3.1.

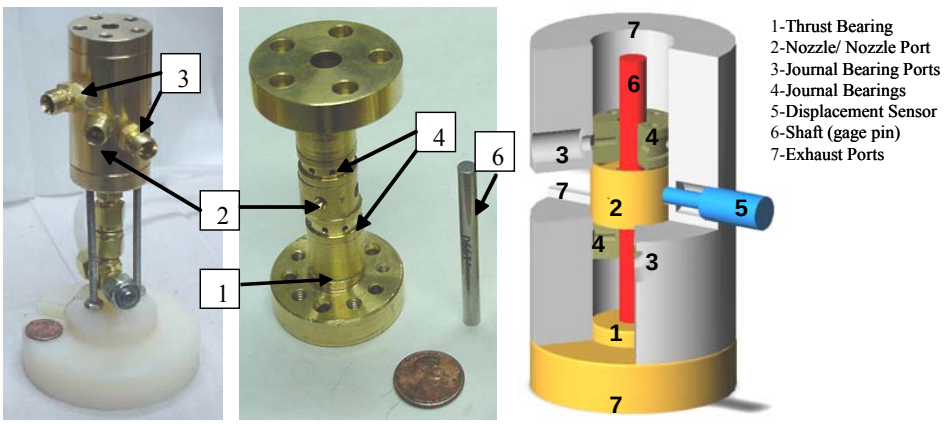

Figure 3.1: Test Facility

3.1.1 Hydrostatic Journal Bearings

Figure 3.2 shows a solid model of the prototype bearings and Figure 3.3 shows the design drawing. The bearings have several manufactured features that include a centered air manifold groove, axial holes for venting, and fillets on all edges. The centered groove allows all feedholes to be pressurized from one source. The axial holes allow the pressure to equalize on each side of the bearing so that axial forces on the bearing are minimized. The groove and axial holes were designed to minimize pressure drop and

manufacturing costs. Knowing the mass flow rate and density of gas supplied to the bearings, and assuming steady state operation and an acceptable pressure drop, the required geometry of the axial holes and air manifold groove can be calculated as follows.

$$\Delta P = \frac{1}{2} \cdot K \cdot \frac{\dot{m}^2}{\rho \cdot A^2} \tag{12}$$

Diameters less than 0.0625" for the air manifold groove caused unacceptable pressure drops (greater than 0.25 psig) so 0.0625 was chosen. The diameters of the axial holes (4 per bearing) were specified to be 0.086" (No. 2). The pressure drop through this hole was negligible. Therefore area exiting the bearing housing (8 axial holes) was about 60 times greater than the area entering the bearings (16 circumferential supply holes), assuring a minimal pressure buildup between bearings. The fillets were added to the bearing edges to reduce the possibility of mechanical damage as the bearings are inserted into the test fixture.

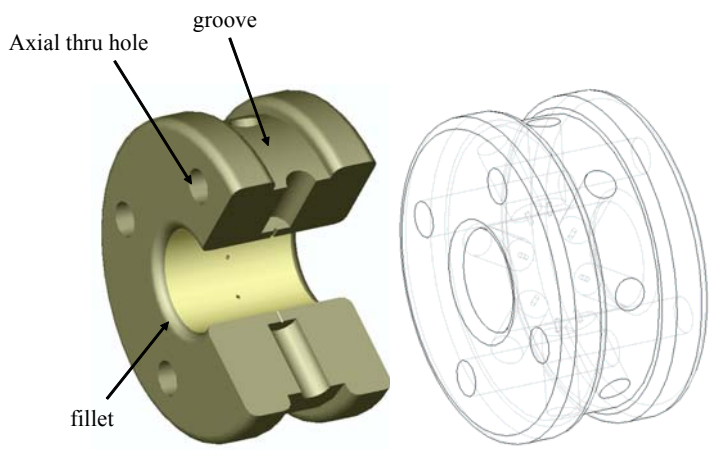

Figure 3.2: Solid model of prototype bearing

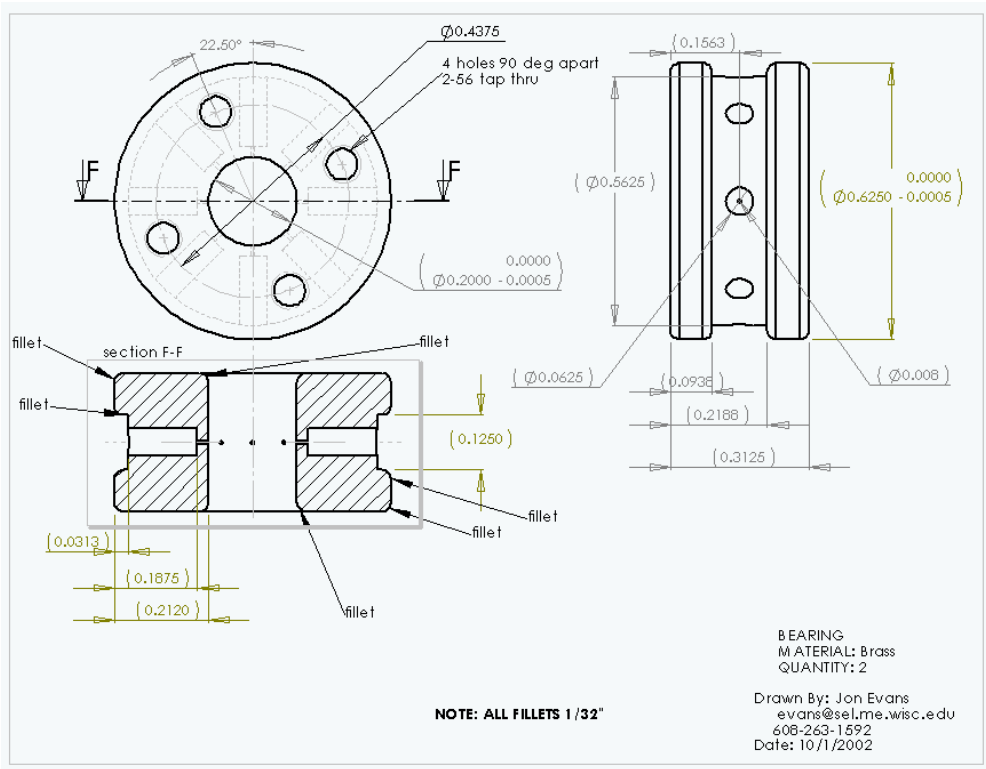

Figure 3.3: Design drawing of bearing

3.1.2 Housing

The housing is the basic component of the test fixture and is shown in Figure 3.4. It includes a bore that allows the assembly (consisting of bearings, spacers, and pneumatic drive) to be aligned. It also serves as a manifolding system for each of the main gas sub-systems (journal bearing, thrust bearing, and pneumatic drive).

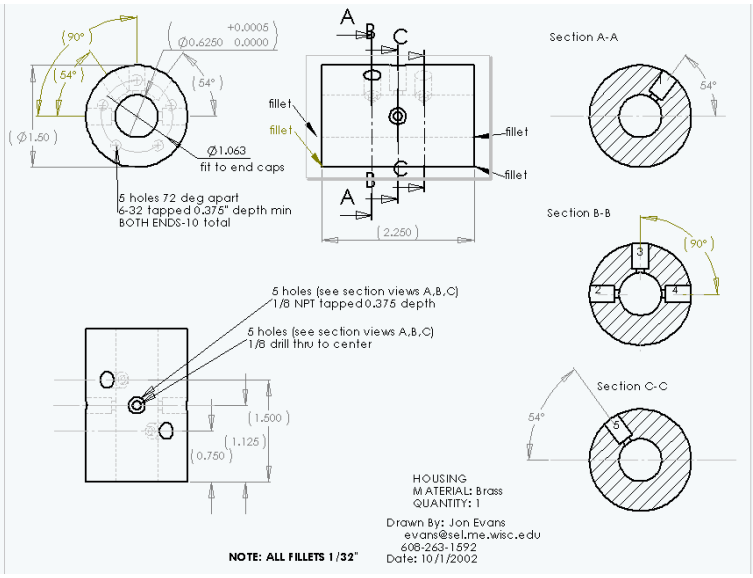

Figure 3.4: Housing body design drawing

Figure 3.5 shows the housing end caps. The bore diameter of each of the end caps was machined concurrently with the outer diameter of the bearings from the same stock. This procedure helped eliminate some misalignment when the test fixture was assembled since the bearings and end caps were machined to have the same diameter without the machine tooling being realigned or the stock being re-chucked into the lathe. The assembly was loaded axially by a wave spring in order for each component to lock up against one another. This helps avoid cocking and motion in response to pressure loads.

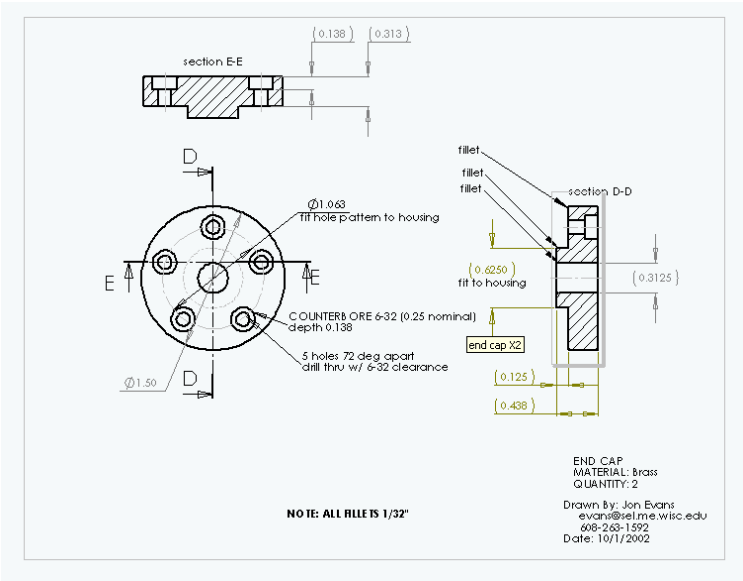

Figure 3.5: Housing end cap design drawing

Figure 3.6 shows an exploded view of the housing and the components required for basic, horizontal operation. Spacers were machined to align the bearings with the supply holes in the housing, but are not shown in Figure 3.6.

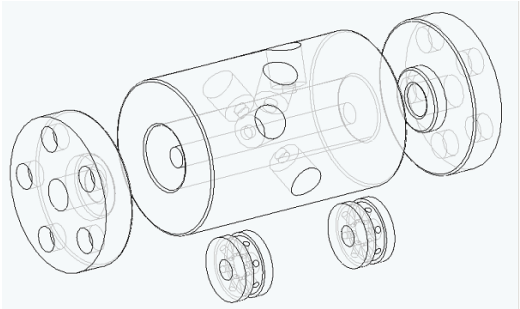

Figure 3.6: Housing with basic components for horizontal operation

3.1.3 Thrust Bearing

The journal bearings support the shaft radially, but for vertical operation the shaft must be supported axially as well. A single inlet, gravity loaded hybrostatic thrust bearing was constructed for this purpose. The supply orifice is centered with respect to

the shaft. The thrust bearing was made in a similar fashion as the end caps. Threaded holes were added that accept threaded rod and to allowed mounting in the vertical orientation, as can be seen in Figure 3.1. Figure 3.7 shows the drawing of the thrust bearing. Figure 3.8 shows the finished thrust bearing. The inlet orifice diameter of the thrust bearing is 0.016 (consistent at a #78 drill). The exhaust hole diameter is 0.0625". Note that the inlet orifice diameter is slightly larger than what was specified in Figure 3.7 (0.016 vs. 0.015). It was modified after experimental trials showed inadequate thrust capacity.

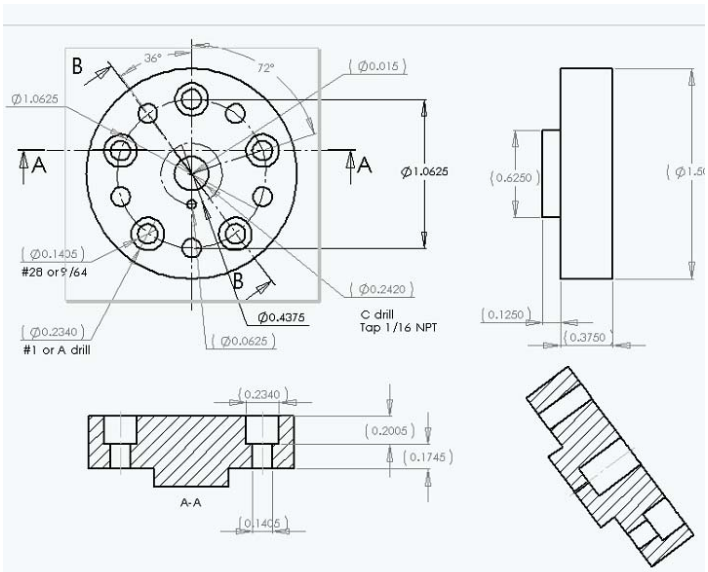

Figure 3.7: Thrust bearing design drawing

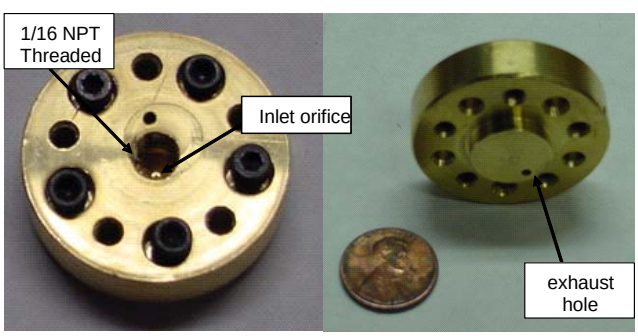

Figure 3.8: Fabricated thrust bearing

3.1.4 Pneumatic Drive

A drive system was designed and fabricated. A nozzle-spacer was designed as a drop-in replacement for the original center spacer. The nozzle outlet lined up with the shaft so that the resulting jet of air would impinge approximately tangentially on the shaft and therefore provide a driving torque. The recessed areas of the nozzle prevented it from blocking the bearing through-holes. This prevented any pressure build up on the interior side of the bearings. Figure 3.9 shows the nozzle-spacer drawing and Figure 3.10 shows the finished nozzle-spacer.

The nozzle diameter is 0.0250" and was installed on a mill with a rotary table. This nozzle diameter is larger than what is shown in Figure 3.9 because smaller drill bits had very short shanks; the clearance between the tooling and the workpiece did not allow for the specified hole to be drilled. To drill the hole, the rotary table was inverted. The mill table was centered on the hole location and the table offset by the radius of the shaft. Finally the rotary table was dialed to an angle of 18.5°, as specified in Figure 3.9.

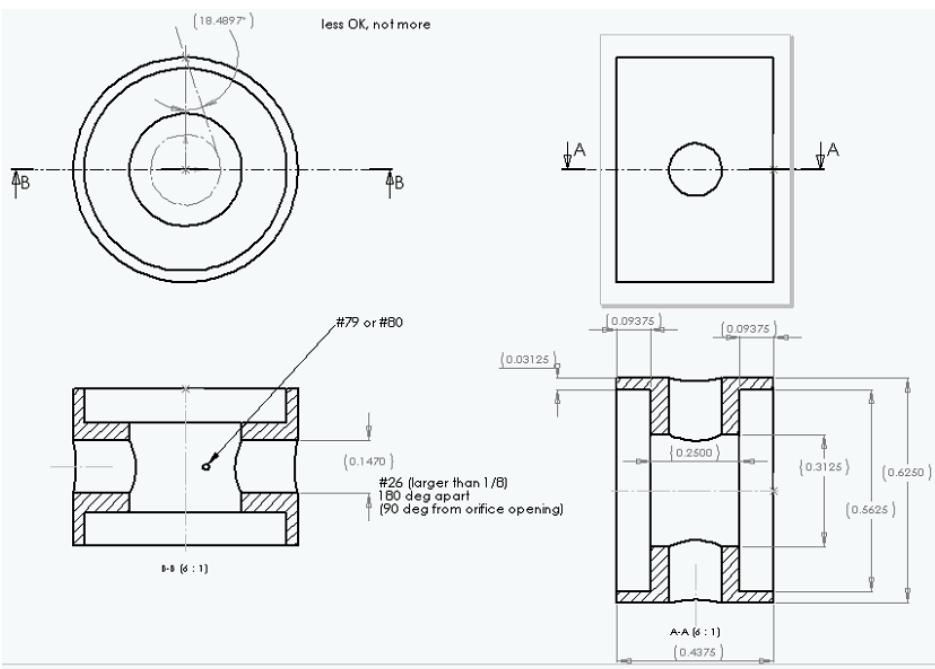

Figure 3.9: Nozzle-spacer drawing

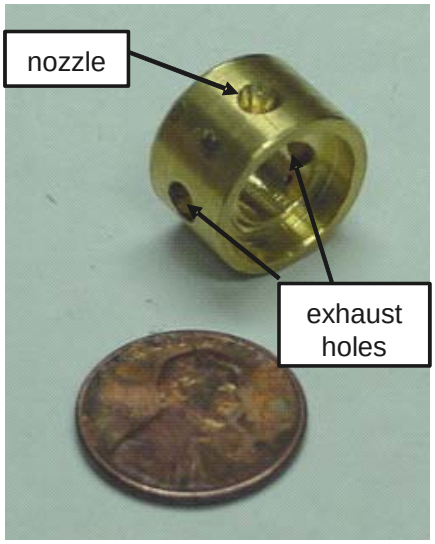

Figure 3.10: Fabricated nozzle-spacer

3.2 Instrumentation

The radial position of the shaft was monitored using a fiber-optic displacement sensor (*Philtec* Model RC 12-C1R), the mass flow rate to the bearings was monitored with a calorimetric flow meter (*Cole Parmer* 32711-48), and the supply pressures for both journal bearings, the thrust bearing and the system exhaust pressure were monitored with 4 pressure transducers (*Omega* PX302-5006V). The bearings were energized with a clean and dry supply of air and the desired supply pressure was set using a pressure regulator. The exhaust pressure could be controlled by adjusting an exhaust throttle valve. A schematic of this setup is shown in Figure 3.11 and a picture of the experimental setup is shown in Figure 3.12.

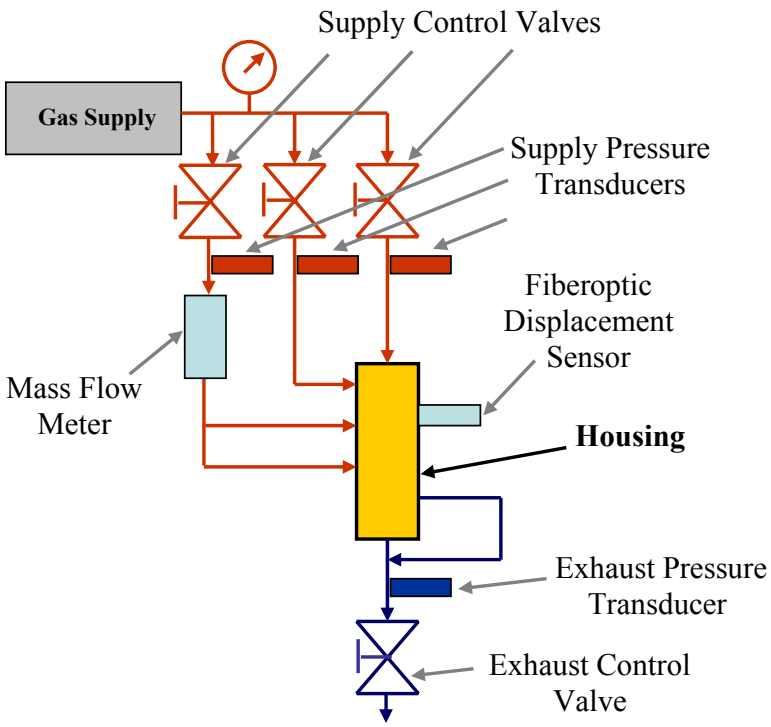

Figure 3.11: Schematic of experimental setup

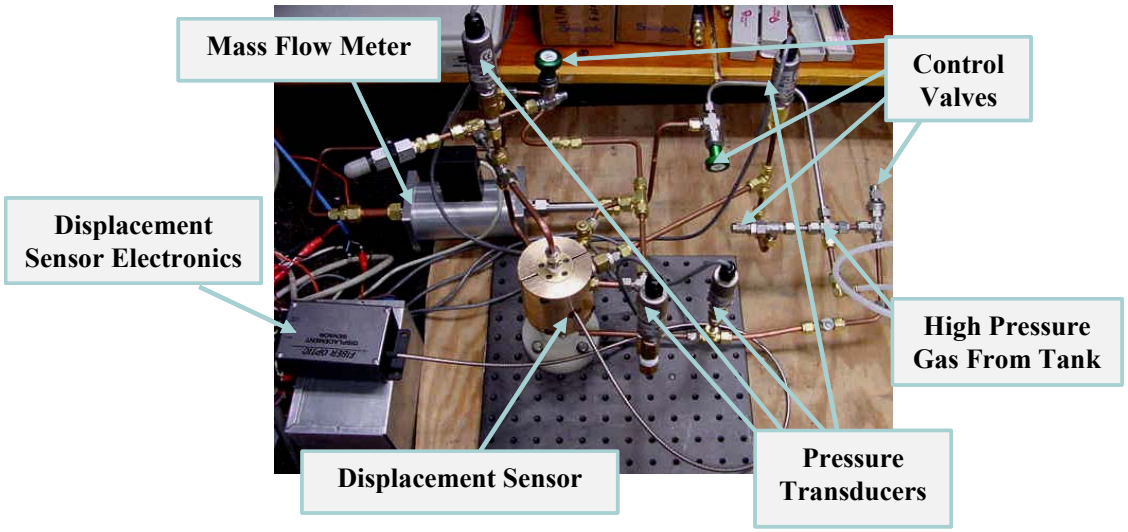

Figure 3.12: Experimental setup

3.2.1 Mass Flow Sensor

The total mass flow rate to the bearings was measured and assumed to be split equally between the two bearings. The *Cole-Parmer* mass flow rate sensor was placed in line with the gas supply. The sensor is compatible with a wide range of gases provided the specific heat capacity is known. Figure 3.13 shows the model 32711-44 sensor, which is a smaller version of the 32711-48 sensor.

Figure 3.13: Typical *Cole Parmer* mass flow sensor

3.2.2 Fiber-Optic Displacement Sensor

In order to determine rotordynamic characteristics such as speed and the shaft-bearing natural frequency (and therefore bearing normal stiffness) it was necessary to utilize a displacement sensor capable of detecting very small shaft motions at a high frequency. Several types of sensors were considered including capacitive and fiber-optic based instruments. A fiber-optic sensor manufactured by the *Philtec* Model RC12 C1R, was chosen for this application.

The *Philtec* fiber-optic sensor has an emitter and a receiver. It measures the delay between light pulses and electronically transforms the delay into an analog voltage. It has special cable sheathing (option C1) constructed of interlocking stainless steel hose that allows the sensor to operate at cryogenic temperatures and provides maximum crush resistance. The sensor uses a narrow band-pass filter centered at 880 nm wavelength (option R) that reduces the effects of ambient light by up to 50 to 100 times. Fiber-optic sensors can be sensitive to surface finish, but the RC models use a second reference signal in order to calibrate reflectance variations out of the measurement (RC stands for

Reflectance Compensated). The sensors resolution (3 μin/ 0.076 μm) and frequency response (20 kHz) are adequate to measure speed, natural frequency, and other rotordynamic characteristics of the system. Figure 3.14 shows a typical fiber optic sensor from *Philtec* and Figure 3.15 shows the typical response of the RC12 fiberoptic sensor model.

Figure 3.14: Typical *Philtec* fiberoptic sensor

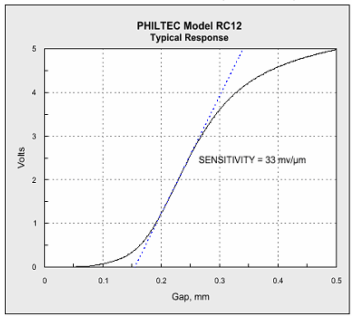

Figure 3.15: RC12 *Philtec* fiberoptic sensor response curve

The shaft was supported axially by the thrust bearing and driven at a speed less than the shaft/bearing resonant frequency using the pneumatic drive system. The natural frequency of the shaft/bearing system (f_n) was measured by imparting an impulse radially on the housing and measuring the frequency of the resulting oscillations. A typical impulse response from the displacement sensor is shown in Figure 3.16. The natural frequency was used to calculate the stiffness (k) of each bearing according to:

$$k = 2 \cdot \pi^2 \cdot f_n^2 \cdot m_{shaft} \tag{13}$$

where m_{shaft} is the mass of the shaft.

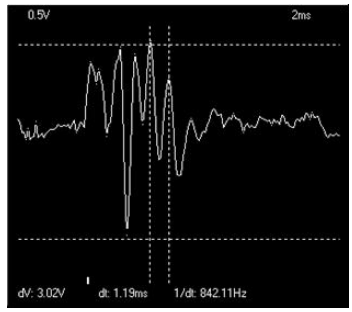

Figure 3.16: Typical impulse response from displacement sensor

The accuracy and repeatability of this technique was improved by carrying out multiple trials with each operating condition and by measuring the time for several (rather than a single) oscillation. Figure 3.17 shows the sensor mounting fixture that was manufactured. The fixture maintains hermeticity at elevated pressures while still allowing the radial motion required for sensor adjustments. An O-ring was seated between the inside of the sensor mounting fixture and the outside of the test fixture. It serves the dual purpose of sealing the test fixture and providing a force (friction between the sensor and the O-ring) in opposition to the elevated pressure that would otherwise tend to push the sensor out of the mounting fixture.

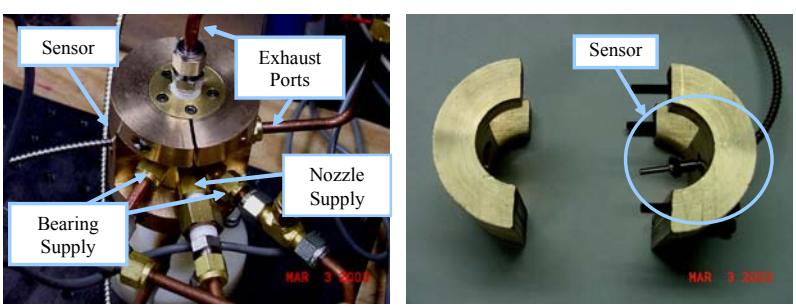

Figure 3.17: Fiberoptic sensor fixture

CHAPTER 4

Experimental Results and Model Validation

This chapter presents experimental measurements and compares them to the model predictions.

4.1 Ambient Exhaust Pressure

The experimental test facility was operated using compressed air with an ambient exit pressure over a range of supply pressures. Figure 4.1 illustrates the mass flow rate measurements (per bearing) and the model predictions for the nominal clearance as well as the upper and lower limits of the possible clearance, based on the estimated manufacturing and inspection accuracy. Figure 4.2 illustrates the measured and predicted stiffness. Note that a correction factor, *cf* in Equation (7), of 0.8 was used, in the calculation of the stiffness, to account for the circumferential interaction between feedholes. The correction factor of 0.8 agrees with empirical values reported by other authors for, for example (Robinson 1958), and also causes this data to compare well with the model predictions.

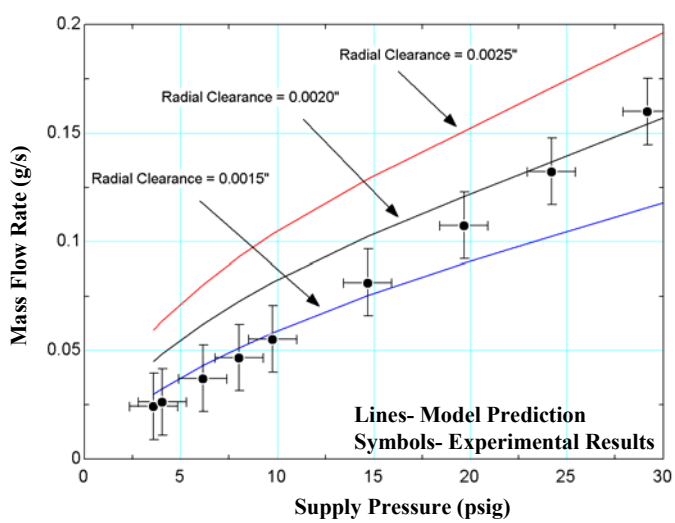

Figure 4.1: Measured and predicted mass flow rate with ambient exhaust pressure

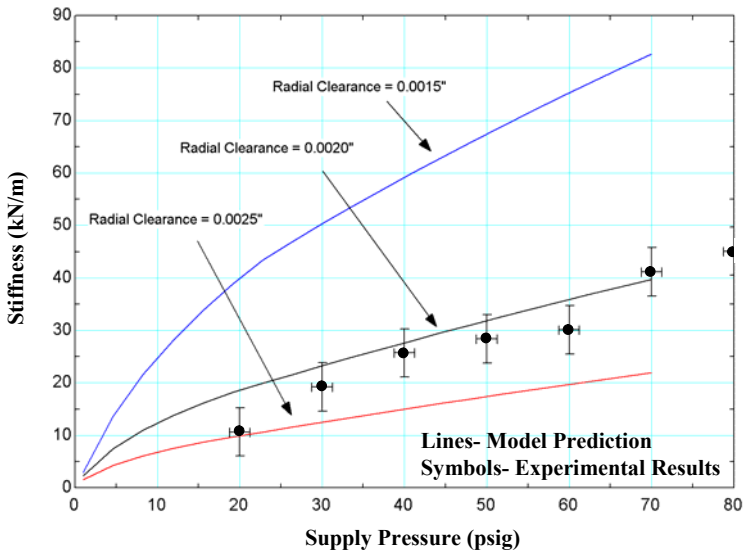

Figure 4.2: Measured and predicted stiffness with ambient exhaust pressure

4.2 Elevated Exhaust Pressure

Figures 4.3 and 4.4 illustrate the measured and predicted mass flow rate and stiffness for a fixed supply pressure as the exhaust pressure is varied. The mass flow rate data was taken at an exhaust pressure of 70 psig while the stiffness data was taken at an exhaust pressure of 60 psig. The same correction factor was used to calculate stiffness.

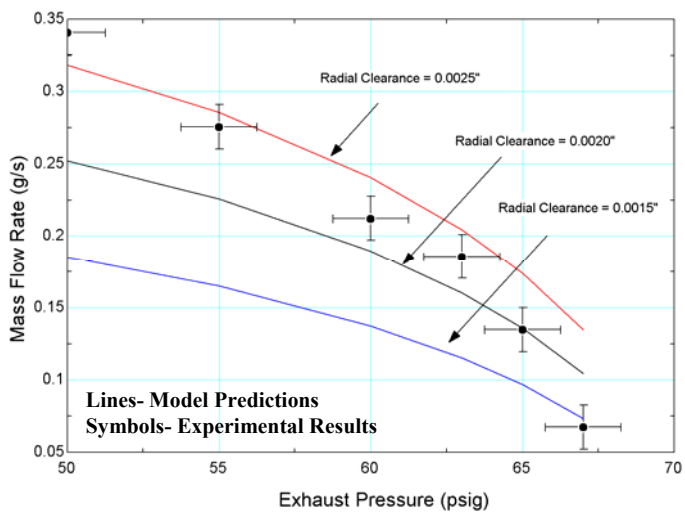

Figure 4.3: Mass flow rate with elevated exhaust pressure (70 psig supply)

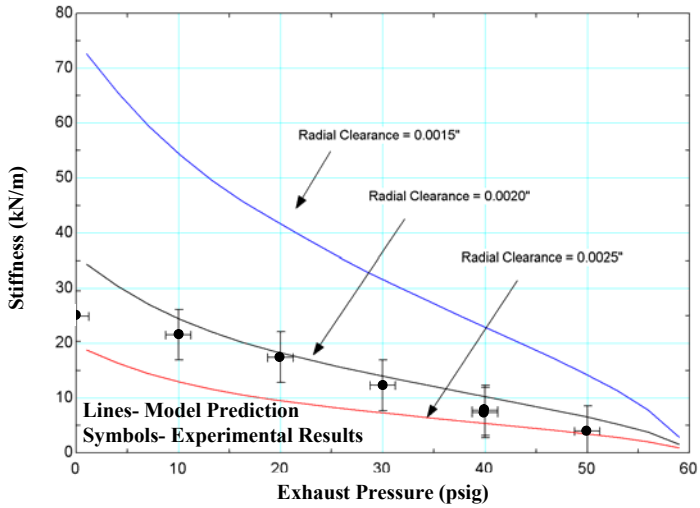

Figure 4.4: Stiffness with elevated exhaust pressure (60 psig supply)

4.3 Scaling Parameters

One important application of the hydrostatic bearing model is its ability to predict the scaling parameters, C_m and C_k, for a particular geometry and operating conditions in order to allow a more complete optimization of the hybrid cryocooler. Figure 4.5 illustrates the locus of the measurements expressed in these coordinates as well as the predicted coefficients for the range of test conditions assuming the nominal clearance.

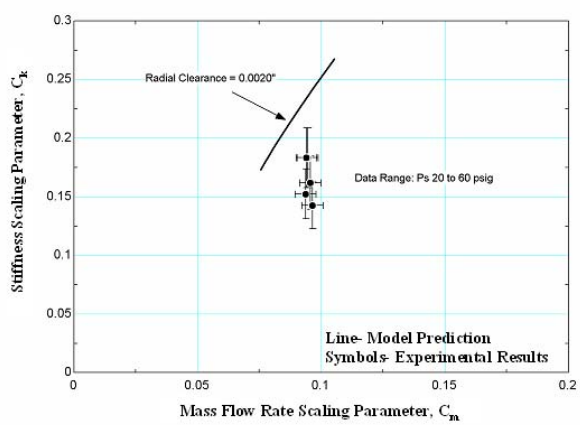

Figure 4.5: Measured and predicted scaling parameters

As can be seen from Figure 4.5 the model consistently under-predicts the stiffness of the bearing but over-predicts the mass flow rate consumption under the conditions considered here.

4.4 Shaft Rotational Speed Measurement

The displacement sensor can be used to measure the rotational speed of the shaft, because it is affected by a groove on the gage pin (see Figure 4.6 - the groove is associated with the diameter etching). The sensor picks up the groove as a change in displacement during each revolution, as can be seen in Figure 4.7. Even without any torque from the nozzle with conditions as shown in Figure 4.7 (a), the shaft spins (at 62.7 Hz; 3700 RPM) due to asymmetries in the thrust and journal bearings and the low viscous drag associated with the hydrostatic support system. The nozzle pressure was increased to 20 psig which caused the gage pin to spin faster (at 313.7 Hz; 18800 RPM) as can be seen in Figure 4.7 (b).

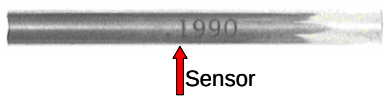

Figure 4.6: Diameter etching on gage pin

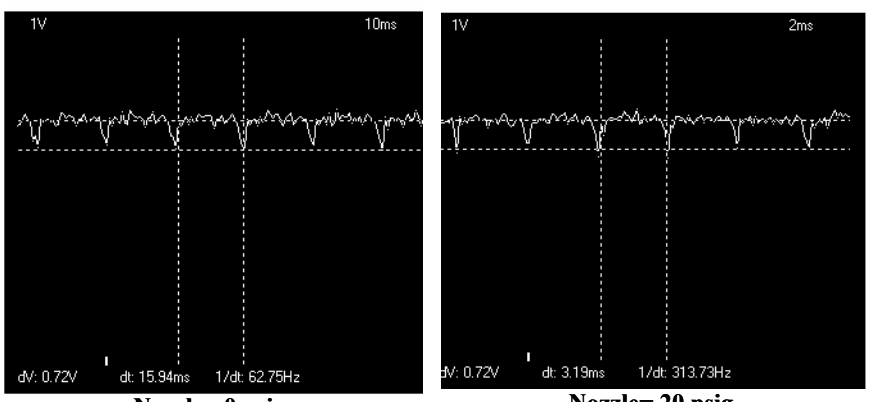

Nozzle= 0 psig
Journal= 20 psig; Thrust= 30 psig
(a)

Nozzle= 20 psig
Journal= 20 psig; Thrust= 30 psig
(b)

Figure 4.7: Typical rotational speed measurement

CHAPTER 5

Bearing Optimization and Research Summary

This chapter describes how the bearing geometry is optimized for the conditions associated with the hybrid cryocooler and explores how the bearing performance effects the hybrid cycle. It also summarizes the research and gives some recommendations for further work relative to bearing testing, including the preliminary design of a more sophisticated bearing test facility.

5.1 Bearing Optimization for Hybrid Cryocooler

The performance of the hybrid cryocooler was found to be sensitive to the characteristics of the hydrostatic bearings, as represented by the scaling parameters C_m and C_k. Figure 5.1 illustrates contours of constant 2nd law efficiency (%) as a function of C_m and C_k for a cryocooler capable of providing nominally 1 W of refrigeration at 10 K and 5 W at 60 K. The 2nd law efficiency is defined as the ratio of the power required by a reversible cryocooler to the actual power loads required by the cryocooler to provide the same refrigeration at the same temperatures. The system model used to generate the efficiency contours was developed in a separate research project (Nellis, 2003). The bearing geometry assumed by the system model is a radial clearance (c) of 0.0005 inch (13 μm), a shaft radius (r_s) of 0.10 inch (2.54 mm), and a bearing length (b) of 0.313 inch (8.0 mm). The remainder of the bearing geometry (e.g. supply hole radius and station position) is optimized in this section. It can be seen from Figure 5.1 that as C_m increases the bearings consume more mass flow resulting in a reduction of system efficiency. As C_k decreases, the achievable rotational speed and therefore aerodynamic efficiency decreases resulting in a loss of system efficiency.

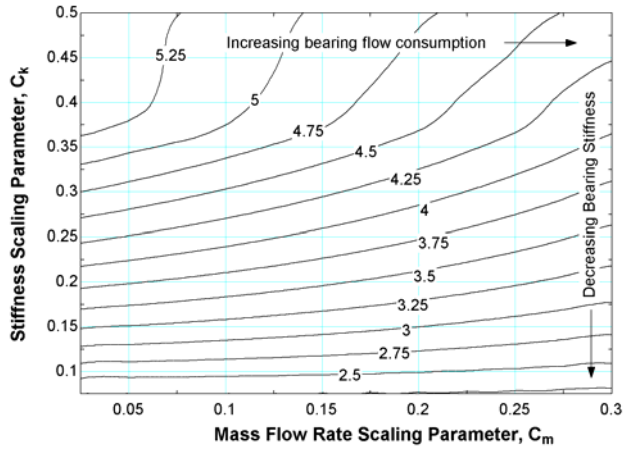

Figure 5.1: 2nd law efficiency (%) as a function of scaling parameters C_m & C_k

An optimal bearing design would maximize system efficiency by varying the remaining geometric parameters: number of supply holes (N), location of supply holes (L/b), and supply hole radius (r_h). The number of feed holes (N) was found to have a weak effect on the bearing performance and therefore a circumferential array of 8 feed holes was chosen. Operating conditions for the hydrostatic bearings were taken to be 60 K helium gas at a supply pressure of 175 psia (1.21 MPa) and an exhaust pressure of 120 psia (0.83 MPa), consistent with the anticipated cycle conditions for an optimally sized linear compressor. The feed hole radius (r_h) and axial distance from the bearing edge to the feed hole (L) were varied as free parameters in order to obtain corresponding values of C_m and C_k using the bearing model, given the constraints described above.

Figure 5.2 shows the locus of predicted stiffness and mass flow rate scaling parameters obtained as the feed hole radius was varied for different values of station, L/b. The results are overlaid onto the 2nd law efficiency (%) contours shown in Figure 5.1 in order to clearly show the optimal bearing geometry.

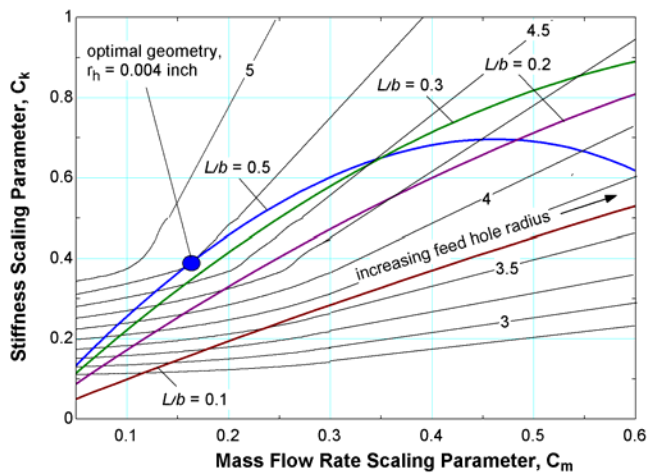

Figure 5.2: Optimization of hydrostatic bearings for the hybrid cryocooler

Notice that the optimal bearing design for the hybrid cryocooler does not maximize the stiffness coefficient as this would result in a prohibitively high value of the mass flow rate scaling parameter. The optimal geometry is a single admission (L/b = 0.5) bearing with a 0.004 inch (0.1 mm) feed hole radius. Double admission bearing designs (L/b< 0.5) can achieve higher stiffness but only at higher mass flow rate (see, for example, L/b= 0.2 in Figure 5.2).

The optimization described previously was accomplished only after assuming a fixed clearance. The specified clearance is based on the anticipated constraints associated with conventional machining processes. This specification is dependent on the accuracy of the tool and the skill of the operator. For a dimension machined on a lathe, such as the radius of the shaft or the inside diameter of the bearing, the lathe runout will determine the precision of the fabricated part. The lathe runout is dependent on the type of bearings installed in the machine (higher quality bearings have reduced runout) and the age of machine (bearings have a limited lifetime and may eventually wear out). Therefore in order to achieve the specified clearance (0.0005"; 13 μm), a lathe with high quality bearings with runout of less than 0.0001" (3 μm) must be used. Keeping the clearance at a minimum is important because stiffness scales inversely with c and mass flow consumption scales inversely with c^3 as can be seen in equations (9) and (10) and Figures

2.23 and 2.24. Because viscous drag is so low and the bearings are at an elevated temperature (relative to the refrigeration load) temperature, the optimal clearance will always be far less than what can be manufactured with conventional technology. Figure 5.3 illustrates the predicted 2nd law efficiency (%) of the hybrid cryocooler as a function of the radial clearance using the scaling parameters predicted by the model for the optimal bearing design shown in Figure 5.2.

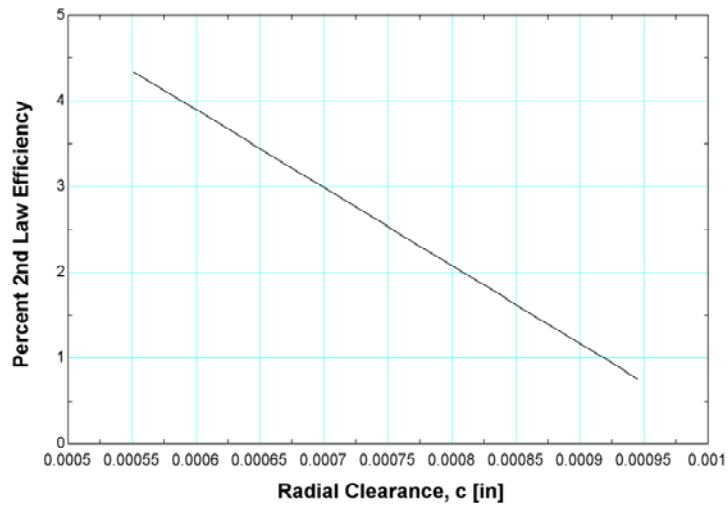

Figure 5.3: 2nd Law Efficiency (%) vs. radial clearance in the hydrostatic bearings

It can be seen from Figure 5.3 that the shaft-bearing clearance has a significant effect on the system performance and that the cycle is not practical for radial clearances greater than 0.001" (26 μm).

5.2 Bearing Research Summary

A hybrid cycle that combines a pulse-tube upper stage with a reverse-Brayton lower stage is being developed. The performance of the hybrid cryocooler was found to be strongly dependent on the characteristics of the hydrostatic bearings needed to support the cryogenic turbine in the reverse-Brayton stage because both the mass flow consumption and the stiffness of the bearings are direct penalties on cycle performance. A hydrostatic bearing model was developed that allowed the stiffness and mass flow

consumption to be predicted as a function of gas properties, operating conditions, and bearing geometry. Scaling parameters for both stiffness and mass flow consumption are used to interface the bearing model with an overall hybrid system model.

It was found that an optimized bearing design did not maximize stiffness since this would require a high mass flow rate which would result in a net loss of cycle performance. Rather, in the optimized design, some stiffness was sacrificed in order to greatly reduce the mass flow consumption. Likewise it was found that single admission bearings (L/b=0.5) were optimal for the hybrid cycle since this design minimizes mass flow consumption for a given stiffness. These effects were illustrated in Figure 5.2 where the scaling parameters were superimposed over cycle efficiency contours. The clearance between the turbine shaft and bearings was found to be of critical importance to the overall cycle efficiency and this trend was illustrated in Figure 5.3.

5.3 Recommendations for Further Bearing Research

Since the clearance between the turbine shaft and the hydrostatic bearings is such an important parameter on overall cycle efficiency it should be a key focus of future design and fabrication efforts. The clearances involved are small (nominal radial clearance of 0.0005" or 13 μm), but can be achieved with standard machine shop tooling and practices. It is important to remember that although the clearances are small, they are still larger than those associated with other types of bearings suited for this application, such as hydrodynamic bearings.

Furthermore hydrostatic bearings are simple and reliable. These characteristics will mean that the hydrostatic bearings will be less costly to manufacture and their use will yield a more robust cryocooler. Future research should focus on the design and fabrication of a turbine shaft system, with careful attention to fabrication techniques that will reduce the shaft-bearing clearance without sacrificing the afore-mentioned advantages. Future research should also result in testing hydrostatic bearings at cryogenic temperatures and high pressures using helium gas in order to validate this model at more prototypical conditions. The hydrostatic bearing model should be refined to include interactions between equivalent slots (beyond a correction factor as used

currently). This will require a full 2-D solution to the Reynolds equation over each bearing pad.

5.4 Generation II Gas Bearing Test Facility

A more precise method of measuring bearing rotordynamic coefficients is being explored through the development of a generation II gas bearing test facility. This facility will allow advanced bearing designs to be evaluated more effectively. A conceptual drawing of the generation II test facility is shown in Figure 5.4.

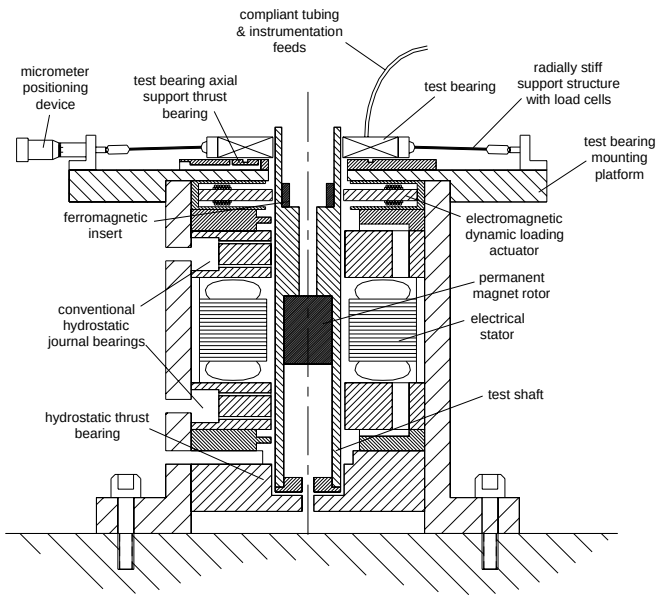

Figure 5.4: Generation II gas bearing test facility

The test shaft is supported radially using two conventional hydrostatic journal bearings of large size and clearance in relation to the test bearing. Axial support of the shaft will be provided by a simple hydrostatic thrust bearing that acts against the weight of the shaft. The journal-thrust bearing set will be setup similar to the generation I test facility. The generation II test facility will not use gage pins; instead, a more advanced shaft described in this thesis will be designed with a permanent magnet embedded into its center. An electromagnetic drive system will allow accurate measurement and precise

control over the rotational speed of the shaft during testing and will help minimize the uncertainty in the measured coefficients. The generation II test facility will dynamically load the shaft by applying an oscillating force at the position just below the test bearing. The loading will be accomplished using opposing electromagnets acting on a ferromagnetic insert in the shaft. The frequency and direction of this loading can be precisely controlled and the loading frequency can be different from the driving frequency.

The mounting and instrumentation of the test bearing is shown in Figure 5.5. This mounting mechanism will yield precise control over the position of the test bearing so that it may be placed in any static position relative to the shaft prior to applying the dynamic loading; thereby allowing the effect of eccentricity on the rotordynamic coefficients to be investigated. The generation I test facility does not have this capability, whereas the generation II test facility will be able to accomplish this by utilizing 2 micrometer heads mounted to the base of the test facility housing as shown in Figure 5.6.

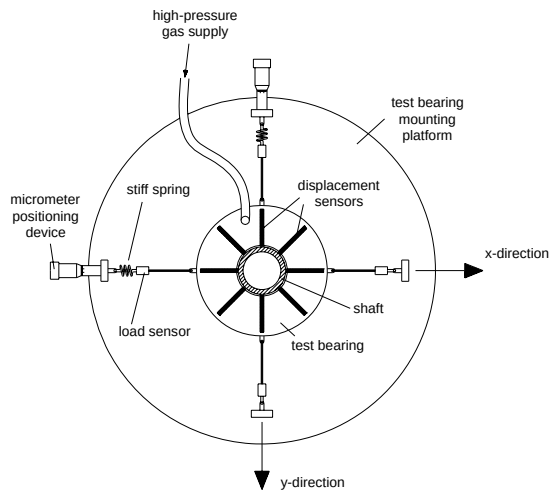

Figure 5.5: Mounting and instrumentation of test bearing

Incorporated in the mounting mechanism will be high resolution load cells capable of measuring the orthogonal forces imported on the bearing. The bearing and housing will be made of aluminum to minimize the effect of acceleration on these forces. The relative

position of the bearing with respect to the shaft will be measured by an array of small displacement sensors. Simultaneous measurement of the relative displacement and force along the orthogonal axes will allow computation of the dynamic stiffness (normal and tangential) and damping (normal and tangential) as a function of the excitation frequency.

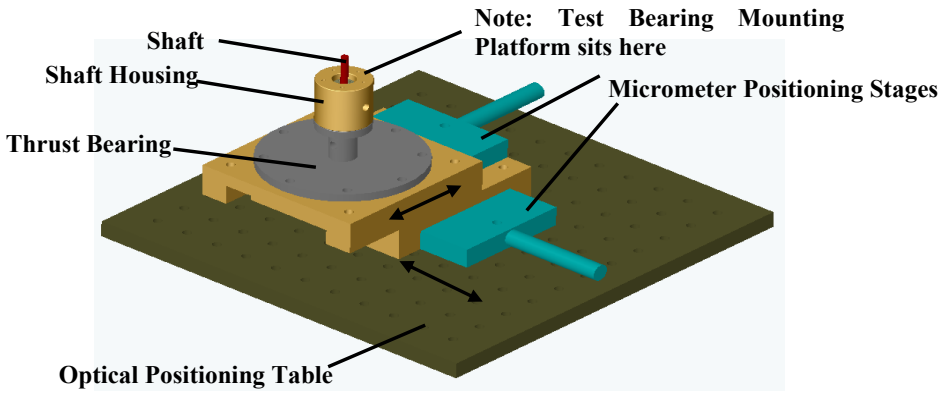

Figure 5.6: Partial 3-D model of generation II gas bearing test facility

CHAPTER 6

Preliminary Work towards Development of a Hybrid Cryocooler Brassboard

As already mentioned, the hydrostatic bearings are a subcomponent of one component in a larger system; the hybrid cryocooler. This chapter describes work that has been accomplished in order to develop a prototype of the hybrid cryocooler. It specifically details work to design and fabricate the vacuum chamber and its corresponding support structure.

6.1 The Brassboard Concept

The technical objective of the current research is to demonstrate a closed system hybrid cycle operating at nominal temperatures and pressures. A brassboard cooler was proposed based on the prototype hybrid designed previously (Diab, 2003; Nellis, 2002). The brassboard cooler concept will be the result of several past and future research efforts, summarized in Figure 6.1.

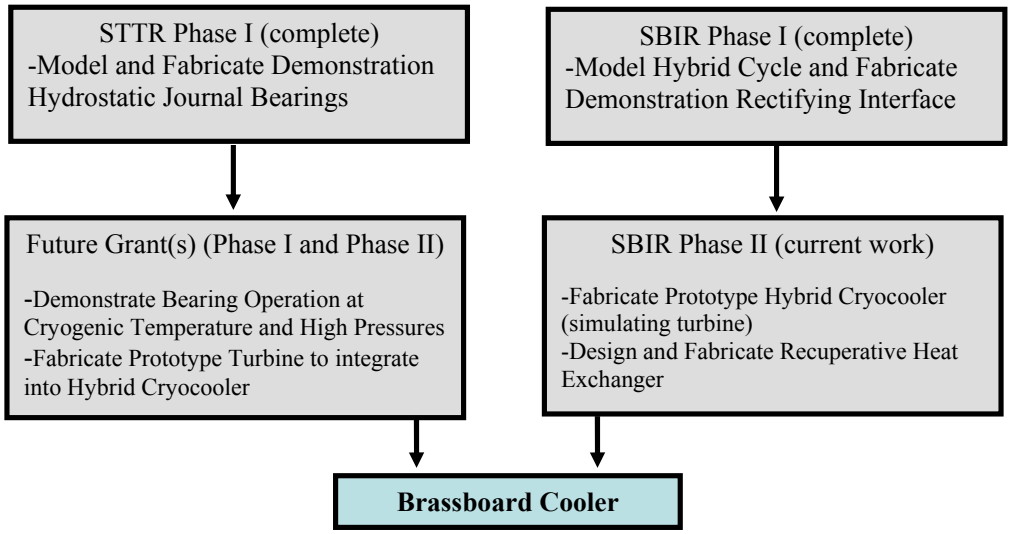

Figure 6.1: Hybrid cryocooler research organization

There are four main components to a fully developed hybrid cryocooler: pulse-tube, rectifying interface, turbine, and recuperator. The development of a pulse-tube (and its corresponding components such as a linear compressor and regenerator) as well as the rectifying interface and recuperator are the current research focus. A heat exchanger/valve combination operating with liquid helium (LHe) will be used to simulate a fully functional turbine. Previous work on the pulse-tube and rectifying interface has addressed many of the technical issues associated with their development. Work on the reverse-Brayton stage will be focused on developing a full-scale recuperative heat exchanger having the required effectiveness ($0.990 < \varepsilon < 0.995$) and the characteristics of low mass and high reliability. The brassboard will be designed to accept a turbine in the event that funding is obtained for further research (as outlined in Figure 6.1) as well as to allow component level testing of the pulse tube, recuperator, etc. A conceptual drawing of the brassboard is shown in Figure 6.2.

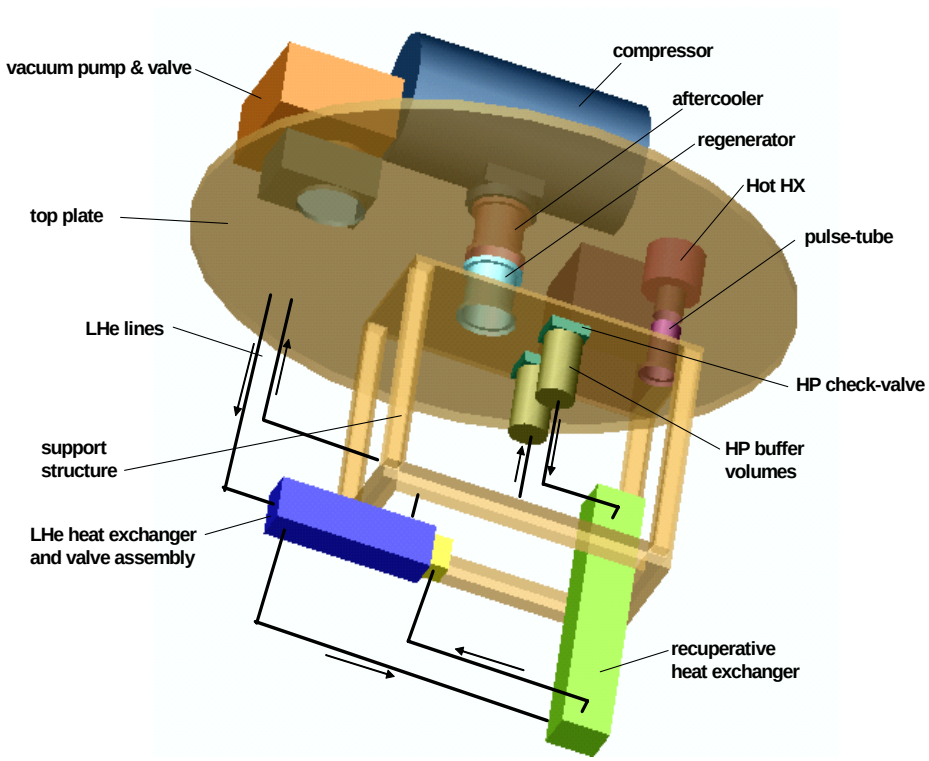

Figure 6.2: Conceptual drawing of brassboard concept

The brassboard will provide a convenient test bed for the systematic evaluation of subassembly and individual component performance. Furthermore, it will allow for the closed system operating at nominal temperatures and pressures to be demonstrated, and it will demonstrate the hybrid cycle operating with a 5 W load at 60 K and a 1 W load at 10 K.

6.1.1 Brassboard Design Iteration 1

The brassboard design has gone through several iterations. In the first design iteration, shown in Figure 6.2, the compressor and aftercooler were to be mounted outside the vacuum vessel on the cover plate. The vacuum vessel was a Dewar and the cover plate was on top of the assembly. The vacuum vessel contained both stages of the hybrid cooler: the pulse-tube stage and the reverse-Brayton stage. The pulse-tube stage was to be constructed in a u-tube configuration, with the cold heat exchanger providing the connection between regenerator and pulse-tube while simultaneously providing a platform for the buffer volumes and check-valves that comprise the rectifying interface that links the 2 stages thermodynamically. The pulse-tube stage was to be supported by the cover plate; thus, the cover plate would serve as the interface between the regenerator and aftercooler, as well as, provide a vacuum boundary through which the hot heat exchanger of the pulse-tube stage would pass.

The reverse-Brayton stage would be supported by the pulse-tube stage, with the potential for additional support structure attached to the cover plate (depending on heat leak versus mechanical stability tradeoffs). It would consist of a recuperator, LHe heat exchanger/valve combination to simulate the turbine, and associated plumbing.

Provisions were made in the cover plate for LHe supply and return lines as well as liquid nitrogen (LN2) supply and return lines. The LN2 was to be used for radiation shielding. The cover plate contained a vacuum pump port, provisions for vacuum gauges, a relief valve, and hermetic cable connectors for data acquisition.

Finally, to make the apparatus as flexible as possible, the various stages were to be interconnected using stainless steel tubing and VCR fittings. Metal-gasket, high-pressure, demountable fittings would enable the interchange of components, instrumentation, and subassemblies with minimal effort.

6.1.2 Brassboard Design Iteration 2

During the preliminary design phase of this project, several modifications were made to the original brassboard design. Shown in Figure 6.3 is a self contained vacuum chamber with its corresponding support structure located at Kirtland Air Force Base in Albuquerque, New Mexico. This type of setup is considered to be more attractive than the configuration described in 6.1.1. The plate is on the bottom instead of the top of the assembly and acts as a baseplate for the assembly.

Figure 6.3: Testing rig at Kirtland Air Force Base

This orientation has several advantages from an assembly viewpoint. It will reduce the time required to service components in the vacuum space. Also, the vacuum canister is moved rather than the cryocooler and cover plate, reducing the possibility of instrumentation/experiment damage and increasing overall accessibility and flexibility. Furthermore, instead of using LN2 as a shield, the recuperative stage will be actively shielded by the cold finger of a closed cycle cryocooler that is attached to a shroud and

mounted to the baseplate. This will allow the recuperative stage to be shielded at various temperatures and reduce the operational complexity associate with a LN2 cooled shield. The main disadvantage will be that this configuration prohibits the use of a u shaped pulse-tube. This means that the hot heat exchanger must be located inside the vacuum space. The heat exchanger will require cooling water with associated vacuum feedthrus. Also, the reverse-Brayton stage will probably have to be attached to the baseplate adding some heat leak to the system. This design was found to be preferable to the first and therefore will be the focus of the following sections which outline some of the details of design iteration 2, specifically the vacuum chamber and vacuum chamber support structure.

6.2 Vacuum Chamber (VaC)

The vacuum chamber consists of 3 main components: the bell jar, feedthru collar, and baseplate. The bell jar has a lifting lug at its apex that allows it to be lifted away from the feedthru collar in order to obtain access to the inside of the chamber. The feedthru collar and baseplate allow instrumentation and other components to be interfaced with the vacuum environment.

The VaC was designed to be flexible in order to accommodate the unknown sizes of the recuperator, compressor, and aftercooler (since the hybrid system has yet to be completely specified). An estimate of the size of the pulse tube and aftercooler was determined and ports were specified to accept these components. The space for the recuperator (inside the vacuum chamber) and compressor (under the baseplate) was maximized and can be adapted to test a wide range of designs.

6.2.1 Design

Several parameters were investigated during the design of the VaC including overall dimensions, space requirements, cost, and the number of feedthrus required for the hybrid cryocooler. This section will address the feedthru issues. The following section will discuss the other design parameters and how they relate to fabrication. Table 6.1 summarizes how many and what types of feedthrus are required.

KF 40 type connections were specified on the feedthru collar. 6” Con Flat type feedthrus were specified on the baseplate as interfaces for the pulse tube/aftercooler, cryopump, and turbo vacuum pump. A KF 40 type connection was specified for the vacuum roughing pump to maximize conductance from the roughing vacuum to the VaC. Extra ports were specified on both the baseplate/feedthru collar to account for extra instrumentation and/or to allow the vacuum chamber to be used simultaneously for another experiment (e.g. component level testing of the recuperative heat exchanger).

COLLAR	feedthru	BASEPLATE	feedthru
Low Vacuum Gage	KF 40	Pulse Tube/Aftercooler	6” thru hole
High Vacuum Gage	KF 40	Cryo Pump for Shroud	6” thru hole
Relief Valve	KF 40	Vacuum Turbo Pump	6” Con Flat
Vacuum Roughing Pump	KF 40		
Up-To-Air Manual Relief Valve	KF 40		
LHe in	KF 40-liquid		
LHe out	KF 40-liquid		
He gas in He gas out	KF 40-liquid (2 lines)		
Water in for Hot HX Water out for Hot HX	KF 40-liquid (2 lines)		
19 pin connector (4-4 wire sensors)	KF 40		
19 pin connector (4-4 wire sensors)	KF 40		
19 pin connector (4-4 wire sensors)	KF 40		
19 pin connector (9 thermocouples)	KF 40		
19 pin connector (9 thermocouples)	KF 40		
19 pin connector (4-4 wire sensors)	KF 40		
Pulse Tube Inertance Tube	KF 40		
Extra	KF 40		
Extra	KF 40		

Table 6.1: Feedthru requirements for vacuum chamber

Figure 6.4 shows a schematic of the aftercooler/pulse tube interface. A 6” con flat Blank will be machined to accept the regenerator and the regenerator will be soldered to the con flat blank. The con flat blank will also be machined with a bolt hole circle and O-ring groove to accept the aftercooler and withstand the design pressure.

Comment [jce1]: NEW DESIGN!!!!

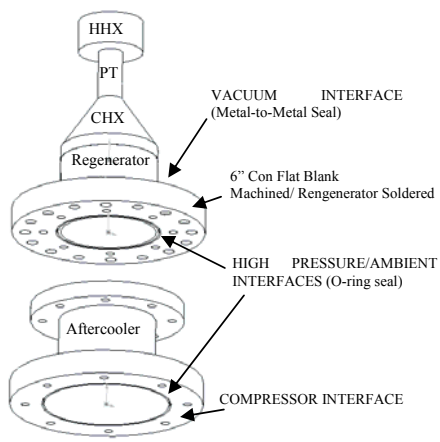

Figure 6.4: Pulse tube/aftercooler interface with VaC

Figure 6.5 shows a schematic of the vacuum system. This configuration will allow the turbo pump to be mounted to the baseplate, the VaC and hybrid cryocooler to be independently leak checked and pumped on, and an access port for leak checking of components independent of the VaC or hybrid cryocooler (for convenience).

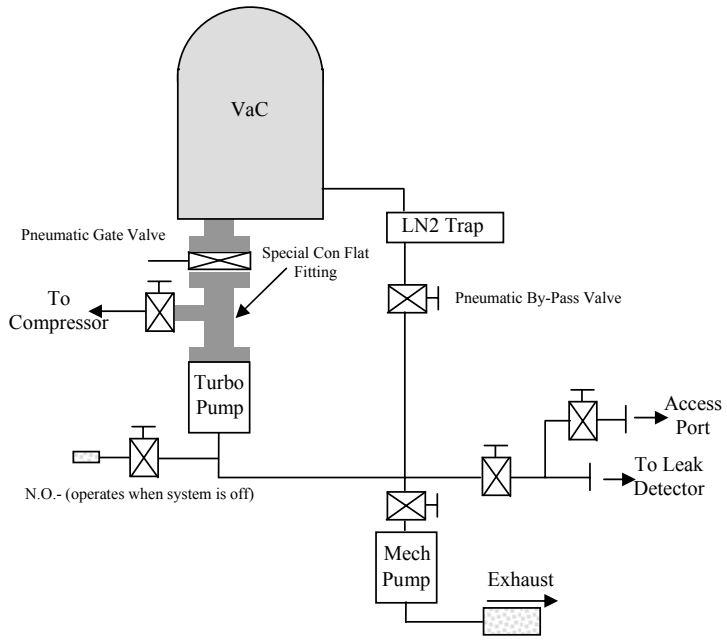

Figure 6.5: Vacuum system schematic for VaC

6.2.2 Fabrication

The VaC was designed to be similar to *MDC Vacuum Products Corporation* (MDC) type bell jar type vacuum chambers due to their extensive experience in manufacturing bell jar type vacuum chambers (https://www.mdc-vacuum.com/). A 30" diameter design was chosen since it was the most cost effective (diameters over 30" have increased costs according to MDC due to material and manufacturing limitations). MDC also makes several standard sizes of bell jars and other overall dimensions were specified to be standard, in order to minimize cost, including:

- bell jar height
- feedthru collar height
- wall thickness of the feedthru collar and bell jar
- flange thickness on both the feedthru collar and bell jar
- O-ring grooves on the feedthru collar and baseplate
- baseplate thickness.

Lifting lugs were also specified for the baseplate and feedthru collar. Figure 6.6 shows a *Solidworks* drawing of the VaC.

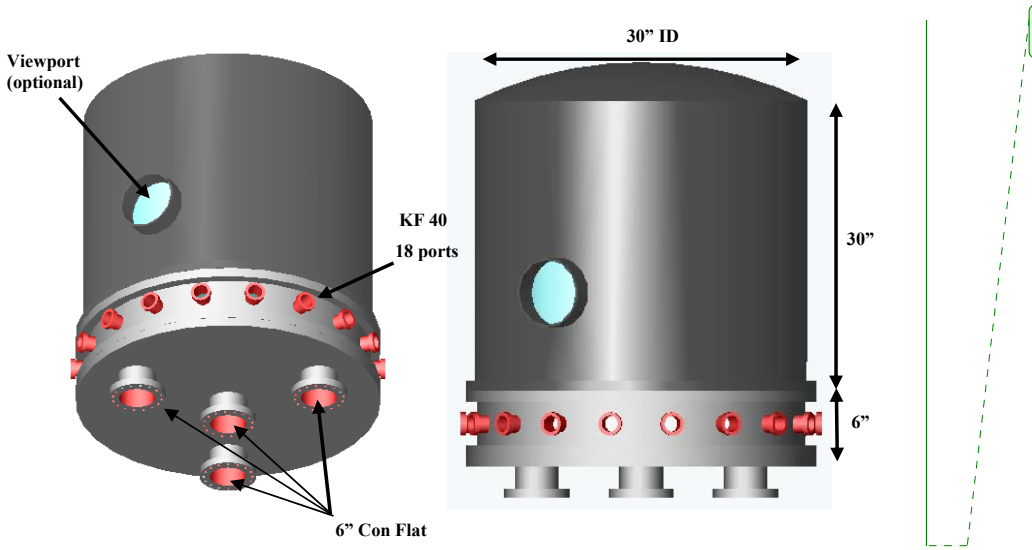

Comment [jce2]: update with new baseplate layout

Figure 6.6: VaC specifications model showing important geometric specifications

Five companies which manufacture custom bell jars are quoting the VAC system including: *MDC Vacuum Products Corp.*, *A&N Corp.* (http://www.ancorp.com/), *Kurt Lesker Co.*(http://www.lesker.com/), *Huntington Mechanical Laboratories Inc.* (http://www.huntvac.com/), and *Nor Cal Products* (http://www.n-c.com/). At this point a manufacturer has not been chosen as all quotes have not been received. The total cost for the VaC is estimated to be between $12,000 and $16,000 (excluding shipping).

6.3 Vacuum Chamber Support Structure (VaCSS)

The Vacuum Chamber Support Structure will allow the VaC to be self contained. It will be aligned under a ceiling crane for assembly purposes as well as to allow the VaC bell jar to be lifted off easily when the system is being serviced. The bell jar can be placed in the upper portion of the VaC for longer term storage (by lifting it with the crane and adding some cross supports into the VaCSS), in order to reduce the lab floor space required and to free up the ceiling crane.

The VaCSS will be constructed of *Unistrut* type members. Although *Fastenal* brand strut will be specified and ordered, it is of identical shape, thickness, and steel gage to *Unistrut* (but less expensive) and therefore beam and column loading data from the *Unistrut* catalog (since it is available, http://www.unistrut.com/) was used for design analysis.

6.3.1 Design

The VaCSS will need to support the VaC, the hybrid cryocooler components inside the VaC, and various auxiliary components attached to the baseplate. Table 6.2 shows a summary of these weights. The VaCSS was designed for static loading. The weight of the VaCSS itself should also be accounted for.

	Weight, lbf	Weight, N
VaC	600	2669
Hybrid Cryocooler	50	223
VaCSS	200	892
Auxillary Components	150	669
Total	**1000**	**4460**

Table 6.2: Vacuum chamber support structure static load requirements

Beam Loading

The beam loading for the 4 short diagonal members (approximately 18" in length, constructed of P100 type strut) is shown in Figure 6.7. The loading was approximated as 4 separate point loads, each taking an equal share of the total system weight. The *Unistrut* catalog lists the maximum allowable point load for the P100 cross section as 845 lbs for a 24" span (18" span is not listed but the max allowable point load would be higher; to the extent that the load is actually distributed this analysis is conservative). The loading for the VaCSS is therefore will within the support strength; this is true even if only 3 of the 4 members provide loading due to misalignment.

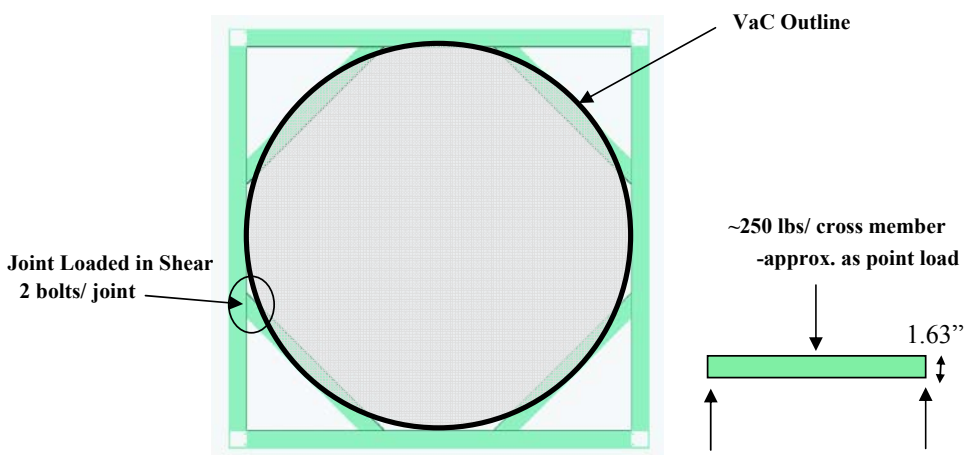

Figure 6.7: Vacuum chamber support structure bolt loading schematic

1/4-20 Grade 8 bolts will be utilized in this design for the VaCSS. The shear yield strength (S_{ys}) for this type of bolt is about 70,000 psi. The shear stress (τ) generated in each bolt is only 637 psi, well within even the most conservative design limits for the load. If the entire load (1000 lbs) was taken by a single bolt (worst case) then the shear stress would still be only ~5100 psi. The calculation is as follows (which assumes even distribution of the load):

$$\tau = \frac{Load}{Area} = \frac{125 \text{ lbs}}{\pi \cdot (.25)^2 \text{ in}^2} = 637 \text{ psi} \qquad (14)$$

The load is then transferred to the outside members (shown in Figure 6.7) through the 8 joints (2 per short diagonal members). The loading of the outside straight members is shown in Figure 6.8.

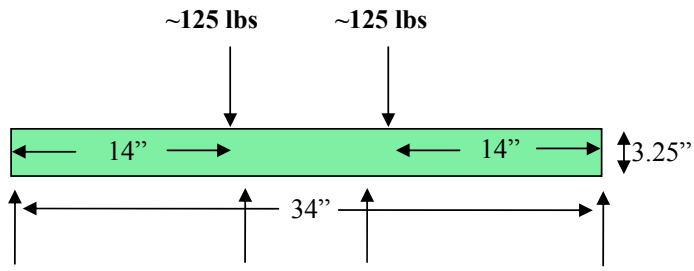

Figure 6.8: Vacuum chamber outside support structure beam loading schematic

The beam loading for the outside straight members (34” in length, constructed of P110 type strut) is shown in Figure 6.8 and was approximated as a point load of 250 lbs. The *Unistrut* catalog lists the maximum allowable point load for the P110 cross section as 1565 lbs for a 36” span. The member is also reinforced with cross brackets 14” from the edge. The loading for the VaCSS is well within design limits; this would be true even if the entire load was supported by 1 of the 4 outside members.

Column Loading

A beam loading analysis was conducted for column loading of the VaCSS. Column members supporting the baseplate will be braced to reduce possibility of buckling failure. Column members attached to the bottom portion of the VaCSS and comprising the upper portion of the VaCSS (as shown in Figure 6.9) will have a maximum span of 48”. When these members are supporting the bell jar (during storage as discussed previously) the maximum load/member will be 75 lbs. The *Unistrut* catalog lists the maximum allowable load in column loading for this span as 2660 lbs.

6.3.2 Fabrication

Shown in Figure 6.9 is a *Solidworks* schematic of the assembled VaCSS with a portion of one of the sides shown in detail. The lower portion of the VaCSS can be assembled

independently of the upper portion. A U bracket connects the upper and lower portions. The system is designed to minimize loading on bolts by placing column members under load carrying beam members (P1001 C Type). These members are further reinforced with 2 cross members per beam members. The entire VaCSS can be bolted to the floor once assembled.

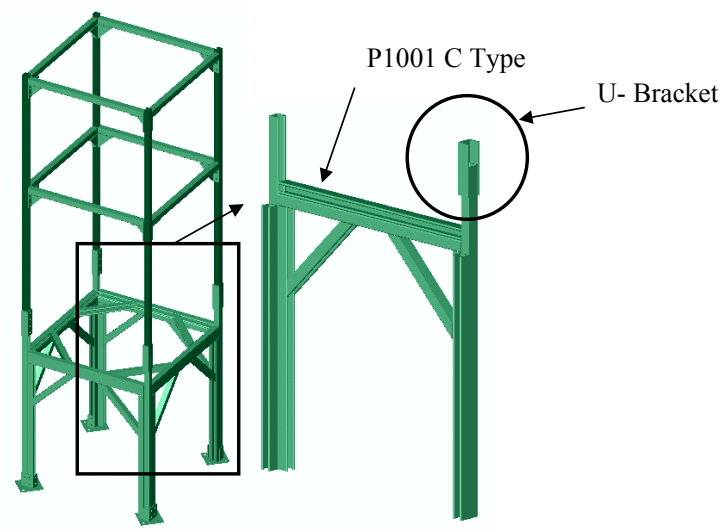

Figure 6.9: Vacuum chamber support structure assembly

Table 6.3 shows a list of required members, fittings, and bolts needed to fabricate and assemble the VaCSS. Strut members are ordered in 10' sections and must be cut to length. *Unistrut* and *Fastenal* catalog numbers are both listed. *Fastenal* does not carry the P1001C type members, but can order it from other suppliers. An alternative to specifying P1001C would be to bolt together 2 P1000/48005 type members that have holes/slots on the side (or drill holes in solid members). The total cost associated with using *Unistrut* members was determined to be about $1420 (excluding shipping) while the cost using *Fastenal* components was about $820 (with free shipping).

Unistrut Part #	*Fastenal* Part #	Part Description	Part Used For	Quantity	Cut To [in]	# 10' sections
P1001C	P1001C	Double Channel	Base Horizontal Support	4	34	2
P1000	48005	Single Channel	Base Vertical Support	8	36	3
P1000	48005	Single Channel	Vertical Corners bottom	4	48	2
P1000	48005	Single Channel	Vertical Corners top	4	72	3
P1000	48005	Single Channel	Middle and Top Supports	8	34	3
P1000	48005	Single Channel	Angle Corners	12	20	3
P2073A	48833	Double Hole Feet	Foot for Vertical Corner	4		
P2226	48721	Wing L	Top and Middle Support	8		
P1377	48755	4 hole U brackets	Connect Top to Bottom	4		
P1325	48691	4 hole L bracket	Vertical Base Supports	12		
P2859	N/A	Frame Caps	Top of Vertical Corners	4		
P2265	48726	45 deg bracket	Cross Piece Horiz. Support	24		
P1010	48604	Channel nut	assembly	100		

Table 6.3: Bill of materials for vacuum chamber support structure

6.4 Future Work

Figure 6.10 shows a *Solidworks* schematic of the assembled VaCSS, VaC, and hybrid cryocooler. Once the VaCSS and VaC are assembled design and testing of hybrid cryocooler components will begin and they will be integrated with the system. Table 6.4 shows a timeline of project milestones and expected completion dates.

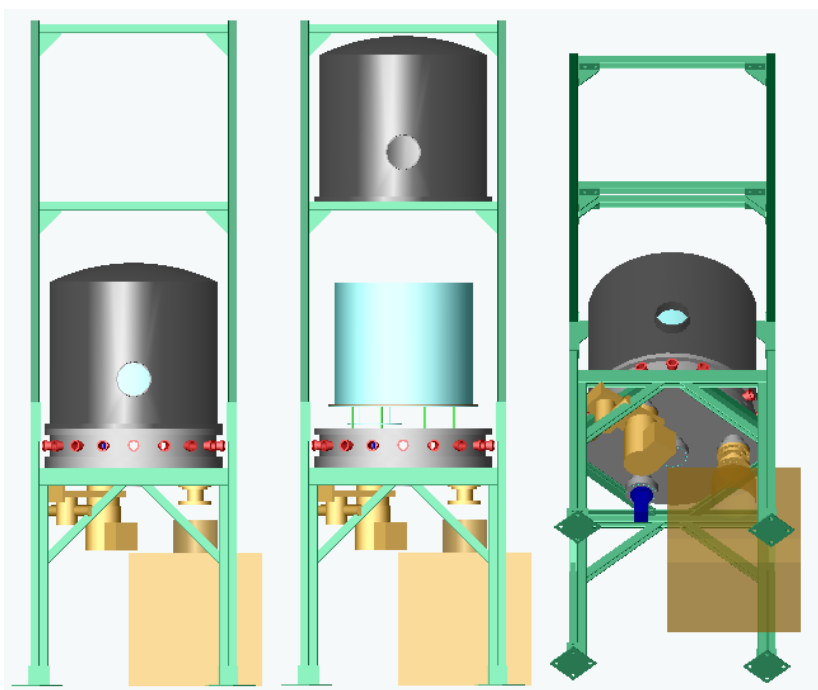

Comment [jce3]: UPDATE W/ new baseplate layout

Figure 6.10: VaC and VaCSS assembly for brassboard cooler

Task	Completion Date							
	Year 1 of Effort				Year 2 of Effort			
	Q1	Q2	Q3	Q4	Q1	Q2	Q3	Q4
Vacuum Test Chamber Design Complete	♦							
Pulse Tube Design Complete		♦						
Vacuum Chamber and Cover Procured		♦						
Compressor Procured			♦					
Aftercooler Procured			♦					
Pulse Tube Components Fabricated			♦					
Pulse Tube Stage Assembled				♦				
Pulse Tube Integrated with Test Chamber				♦				
Pulse Tube Tested				♦				
Rectifying Interface Fabricated				♦				
Recuperative Heat Exchanger Designed				♦				
Rectifying Interface Installed and Tested					♦			
Liquid Helium Heat Exchanger Designed					♦			
Liquid Helium heat Exchanger Fabricated					♦			
Liquid Helium heat Exchanger Installed and Tested						♦		
Full-Scale Recuperator Fabricated						♦		
Recuperator Installed						♦		
Fully Integrated Test Completed								♦
Final Technical Report Completed								♦

Table 6.4: Key project milestones

The following is a more detailed summary of what must be accomplished in order to have a functional vacuum test chamber (the first 1 to 6 months of the project):

- Specification of VaC Stage:
  - Final baseplate design
  - Final VaCSS design
  - Final compressor specification
  - Final pulse-tube and aftercooler design
  - Vacuum Pump System
- Order/Procurement Stage:
  - VaC and VaCSS
  - Flanging/Piping (for VaC and Vacuum Pumping System)
  - Compressor

    - Vacuum Gages/ Electrical Feedthrus/ Liquid Feedthrus
- Assembly Stage:
    - VaCSS
    - VaC
    - VaC Flanging
    - Vacuum Pumping System
    - Vacuum Gages/ Electrical Feedthrus/ Liquid Feedthrus

APPENDIX A

EES Code for Hydrostatic Bearing Model

```
"! NOTE: unit settings:  SI- K, Pa, J, mass basis, radians"
"EES VERSION 6.750 [3/17/03]"

"! INPUT VARIABLES"
"gas characteristics"
gas$='air_ha'          "working fluid"
T_gas=297              "temperature of gas in K"
Pee_gage=0             "gage exhaust pressure in psi"
Pse_gage=10            "gage supply pressure in psi"
pp=14.7                "std atmospheric pressure in psi"
Pse=pp+Pse_gage        "absolute supply pressure of gas in psi"
Pee=pp+Pee_gage        "absolute exhaust pressure of gas in psi"

"bearing geometry"
N=8            "number of supply holes in each row MUST BE EVEN FOR THIS MODEL"
b_e=0.3125     "bearing length in inches"
x=0.5          "location of supply holes along bearing length (ratio of position/total length, L/b)"
c_e=.0020      "centered clearance in inches"
Epsilon=0.1    "shaft offset distance expressed as a ratio of offset distance to centered clearance"
r_se=0.100     "shaft radius in inches"
r_he=.004      "radius of supply holes in inches"
CD=1.0         "supply hole discharge coefficient"
cf=1.0         "correction factor for interaction between equivalent slots"

"! CALCULATIONS FOR MODEL"
"housing, bearing, and shaft geometry conversions to SI for model"
r_s=r_se*CONVERT(inch,m)   "shaft radius in meters"
b=b_e*CONVERT(inch,m)      "width of bearing in meters"
L=(x)*b                    "axial location of supply holes in meters"
c=c_e*CONVERT(inch,m)      "centered clearance in meters"
r_h=r_he*CONVERT(inch,m)   "supply hole radius in meters"
Pe=Pee*CONVERT(psi,Pa)     "exhaust gas pressure in Pa"
Ps=Pse*CONVERT(psi,Pa)     "supply gas pressure in Pa"

L_e=(x)*b_e                "axial location of supply holes in English units"
y=b/(2*r_s)                "length to diameter ratio of bearing"
rp=Pe/Ps                   "overall pressure ratio for duplicate equations"
a_s=(2*PI*r_s*2)/N         "effective slot width-rectangular for duplicate equations"
h_min=Epsilon*c            "h_min cannot be greater than c"

"! PROPERTY CALCULATIONS"
CP=CP(gas$,T=T_gas,P=Pe)                      "constant pressure specific heat"
CV=CV(gas$,T=T_gas,P=Pe)                      "constant volume specific heat"
gamma=CP/CV                                   "ratio of specific heats"
mu=VISCOSITY(gas$,T=T_gas,P=Pe)               "gas viscosity"
rho_gas_exit=DENSITY(gas$,T=T_gas,P=Pe)       "gas density"
MM=MOLARMASS(gas$)                            "molecular weight of gas"
R_gas=(R#/MM)*CONVERT(kJ,J)                   "ideal gas constant"
rcrit=(2/(gamma+1))^(gamma/(gamma-1))         "critical pressure ratio"
```

```
Dtheta=2*PI/N                                   "angular extent of slot"

"! DETERMINE EQUIVALENT SLOT CONDITIONS"
DUPLICATE i=1,N/2
    A_h[i]=2*PI*r_h*h[i]                "effective area for plain jets"
    theta[i]=((2*i-1)*PI)/N             "angle between jet and line connecting bearing and shaft centers"
    theta_deg[i]=theta[i]*CONVERT(rad,degree)      "angle conversion"
    h[i]=c*(1-Epsilon*COS(theta[i]))                "equivalent slot height"

    "mass flow rate calculations"
    m_dot_viscous[i]=a_s*h[i]^3*(pc[i]^2-pe^2)/(24*mu*R_gas*T_gas*L)
    m_dot_inertial_unchoked[i]=CD*(ps/(R_gas*T_gas))*A_h[i]*SQRT(gamma*R_gas*T_gas)*SQRT((g
amma/(gamma-1))*ABS((pc[i]/ps)^(2/gamma)-(pc[i]/ps)^((gamma+1)/gamma)))
    m_dot_inertial_choked[i]=CD*(ps/(R_gas*T_gas))*A_h[i]*SQRT(gamma*R_gas*T_gas)*SQRT((ga
mma/(gamma-1))*ABS((rcrit)^(2/gamma)-(rcrit)^((gamma+1)/gamma)))
    m_dot_inertial[i]=IF(pc[i]/ps,rcrit,m_dot_inertial_choked[i],m_dot_inertial_choked[i],m_dot_inertial_u
nchoked[i])
    m_dot_inertial[i]=m_dot_viscous[i]     "conservation of mass"

    "pressure calculations"
    pmeanv[i]=(a_s*h[i]^3*(pc[i]^3-pe^3)/(36*mu*m_dot_viscous[i]*R_gas*T_gas*L))
    pbar[i]=(L*(pmeanv[i]-pe)+(pc[i]-pe)*(b/2-L))/(b/2)                "mean pressure in slot"
    pc[i]=pe+(ps-pe)*Kg[i]                                             "equivalent slot pressure factor"

    Fn[i]=pbar[i]*b*r_s*(SIN(theta[i]+Dtheta/2)-SIN(theta[i]-Dtheta/2))    "normal restoring force in slot"
END

"! DETERMINE BEARING CONDITIONS"
Fn_tot=SUM(Fn[i],i=1,N/2)*2                          "net normal restoring force"

k\bearing=cf*Fn_tot/(Epsilon*c)                      "stiffness/bearing"
k\bearing_kNpm=k\bearing*CONVERT(N,kN)
m_dot\bearing=2*SUM(m_dot_viscous[i],i=1,N/2)        "mass flow rate/bearing"
m_dot\bearing_gps=m_dot\bearing*CONVERT(kg/s,g/s)

C_m=(m_dot\bearing*mu)/(rho_gas_exit*c^3*(Ps-Pe))    "nondimensional mass constant"
C_k=(k\bearing)*c/((Ps-Pe)*(2*r_s)^2)                "nondimensional stiffness constant"
pr=Ps/Pe                                             "supply to exhaust pressure ratio"
koverm=k\bearing/m_dot\bearing                       "ratio of stiffness to mass flow rate"
```

Solution Window:

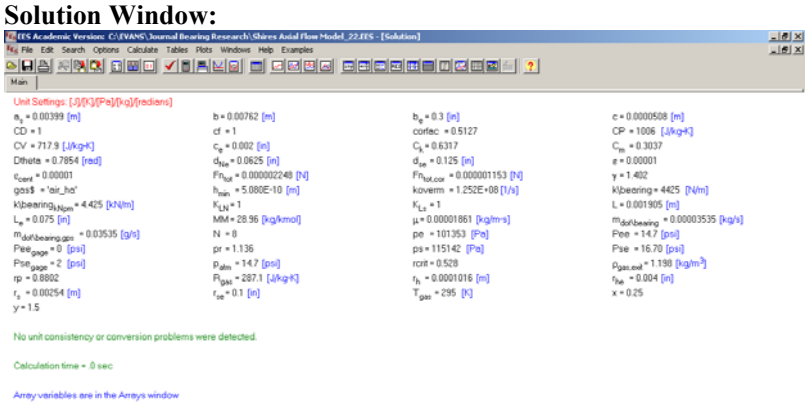

BIBLIOGRAPHY

Crunkleton, J. A., 1993, “A New Configuration for Small-Capacity Liquid-Helium-Temperature Cryocoolers”, *Proceedings of the Seventh International Cryocooler Conference*, p. 187.

Diab, A., 2003, “Modeling and Optimization of a Hybrid Cryocooler”, M.S. Thesis, University of Wisconsin, Madison, WI.

Fay, J. A., 1994, *Introduction to Fluid Mechanics*, MIT Press, Cambridge, MA, p. 566.

Helvensteijn, B. P. M., Kashani, A., Spivak, A. L., Roach, P. R., Lee, J. M., and Kittel, P., 1998, "Pressure Drop over Regenerators in Oscillating Flow", *Advances in Cryogenic Engineering*, Vol. 43, pp. 1619-1626.

Jia, L. X., Wang, L., Addessi, L., Miglionico, G., Martin, D., Leskowicz, J., McNeill, M., Yatauro, B., and Tallerico, T., 2002, "A Five-Watt, G-M/J-T Refrigerator for LHe Target at BNL", *Advances in Cryogenic Engineering*, Vol. 47, pp. 776-781.

Klein, S.A., 2003, EES - Engineering Equation Solver-Version 6.909, F-Chart Software, www.fchart.com

Munson, B.R., Young, D.F, and Okiishi, T.H., 1998, Fundamentals of Fluid Mechanics, 3rd Edition, John Wiley, Ch. 8.

Nellis, G. F., 2003, "A Multi-Stage Hybrid 10 Kelvin Cooler", SBIR Final Report, Contract No. F29601-02-C-0154.

Nellis, G. F., Maddocks, J. R., Kashani, A., J. H. Baik, J., H., and Pfotenhauer, J. M., 2002, “A First Order Model of a Hybrid Pulse-Tube/Reverse-Brayton Cryocooler”, *Proceedings of the 12th International Cryocoolers Conference*, Cambridge, MA, June 18-20.

Powell, J. W., 1970, “Theory of Aerostatic Lubrication”, *Design of Aerostatic Bearings*, Whitefriars Press Ltd, London, Ch. 2, Fig. 2.8, p. 47.

Robinson, C. H., and Sterry, F., “The Static Strength of Pressure Fed Gas Journal Bearings, Jet Bearings”, *A.E.R.E Report R/R 2642*, September 1958.

Shires, G. L., 1964, “The Design of Externally Pressurized Bearings”, *Gas Lubricated Bearings*, Grassam, ed., Burtterworths, London, Ch. 4, pp. 110-139.

Hydrostatic Journal Bearings for a Hybrid Pulse-Tube/Reverse-Brayton Cryocooler

by

JONATHAN CHARLES EVANS

A thesis submitted in partial fulfillment of
the requirements for the degree of

MASTER OF SCIENCE
MECHANCIAL ENGINEERING

at the
UNIVERSITY OF WISCONSIN-MADISON

2003